Research Square

Preprints are preliminary reports that have not undergone peer review.
They should not be considered conclusive, used to inform clinical practice,
or referenced by the media as validated information.

Large-scale In Vivo Profiling Facilitates Systematic Drug Discovery and Repurposing

Xudong Lin

linxd37@mail.sysu.edu.cn

Sun Yat-Sen University https://orcid.org/0000-0001-5479-4414

Yajing Zhou

Sun Yat-Sen University

Kangjian Jiao

Sun Yat-sen University

Guanming Lin

Sun Yat-sen University https://orcid.org/0009-0006-4235-8264

Jiaman Xu

Sun Yat-sen University

Xin Duan

Sun Yat-sen University

Kangdi Zheng

Guangdong Pharmaceutical University

Junhan Duan

Sun Yat-sen University

Jiaying Zhuang

Sun Yat-sen University

Yue Zhao

Sun Yat-sen University

Bingzhe Xu

Sun Yat-sen University https://orcid.org/0000-0003-3007-5655

Zhao Zhang

Guangdong Pharmaceutical University

Tao Chen

Center of Human Microecology Engineering and Technology of Guangdong Province

Honglin Li

Innovation Center for Artificial Intelligence and Drug Discovery, School of Pharmacy, East China Normal University https://orcid.org/0000-0003-2270-1900

Article

Keywords:

Posted Date: November 24th, 2026

DOI: https://doi.org/10.21203/rs.3.rs-11797074/v1

License: This work is licensed under a Creative Commons Attribution 4.0 International License.
Read Full License

Additional Declarations: There is **NO** Competing Interest.

Abstract

Modern drug discovery and repurposing rely heavily on large-scale phenotyping of small animals, which desires rapid animal immobilization, behavioral monitoring, and specific-organ imaging. Despite the recent development of automated *in vivo* screening technologies, the integration of these modalities in a single functional platform remains a challenge. Here, we demonstrate a droplet-based microfluidic platform that enables highly multiplexed *in vivo* profiling of compounds in a large number of animals. This platform employs air-plugs to capsule single zebrafish larva in the droplets and combines microfluidic trapping arrays to enable high-throughput and high-content drug screening. Using this system, we temporally record the whole-brain activities of animals, resulting in a dataset comprising more than 10,000,000 brain images of zebrafish larvae including 1,000 drug conditions. Coupling with machine learning, we provide a novel foundation to identify anti-Parkinson-like drug leads, which have been preliminarily validated in various animal disease models in this proof-of-concept study. It is believed that the proposed fish-in-droplets platform and machine learning-based large-scale profiling approach can pave the way for the rapid identification and validation of novel therapeutic candidates for neural disorders.

Introduction

Neurodegenerative diseases are major public health problems affecting millions of people and becoming the leading causes of death worldwide[1]. Despite tremendous efforts that have been devoted to developing more effective treatments, most of the approved drugs are partially effective for patients with brain diseases, including depression[2], schizophrenia[3], epilepsy[4], and Parkinson's disease (PD)[5]. Given that these disorders are polygenic in origin, single drugs with highly complex pharmacological profiles or polytherapy utilizing multiple drugs are widely employed in the clinical treatments of many neurodegenerative diseases[6]. Thus, discovering mono/polytherapy that interacts with diverse molecular targets might lead to new and more effective medications for a variety of nervous system disorders and has been of interest for a long time.

Nevertheless, the intrinsic challenges of drug discovery and repurposing have substantially limited therapeutic innovation, with few novel mono/polytherapy for neurodegenerative diseases successfully developed in the past decades. This stagnation can be attributed to multiple critical factors, including the limitations of current screening technologies, the lack of *in vivo* drug profiles, and the inherent complexity of biological data mining. These barriers collectively hinder the identification of effective therapeutic candidates. Current pharmaceutical discoveries are often limited by their reliance on overly simplified experimental systems, such as *in vitro* cell-based screening assays, which are extremely difficult to recapitulate the complexity of the vertebrate nervous system and further fail to predict therapeutic outcomes in the human body[7]. Since rodent models with sufficient biological complexity are too unwieldy for high-throughput discovery, various technologies have evolved recently to enable *in vivo* large-scale screening of drugs in small whole organisms, such as zebrafish, to overcome this limitation[8].

For example, a high-throughput platform coupling with a high-speed light-sheet microscope was demonstrated to rapidly assess the effects of drugs on the brain activity of zebrafish[6]. Although such a system was powerful, the high cost, complex external systems, and limited throughput restricted its applicability. Recently, we also developed a fish capsule system that combined automated zebrafish encapsulating technology and machine learning-based prediction strategy for *in vivo* functional screening of mono/polytherapy[9]. However, animals in this platform were capsuled in the agarose gel and the behavioral evaluation was prohibited. Moreover, the preparation of the fish capsules required several processes, which was also inefficient. Despite substantial progress having been made to develop high-content *in vivo* screening systems, functional prediction and validation strategies, integration of these functionalities into a single platform continues to be a technological challenge. Therefore, a cost-effective and highly efficient system for *in vivo* deep phenotyping, prediction and validation using zebrafish to rapidly identify the system-modulating mono/polytherapy is attractive and yet to be achieved.

In recent years, advances in artificial intelligence (AI) have generated powerful tools for multiple stages of drug development from drug design and screening to clinical trials. These innovations not only accelerated the analysis of multidimensional data but also enabled the extraction of insights from highly complex information[10–13]. Without relying on existing pharmacological foundations, AI can perform machine learning or deep learning on vast databases of drug interactions, identifying subtle or intricate functional characteristics and thereby providing technical feasibility for novel drug discovery[10, 13]. However, the existing knowledge (e.g., signaling pathways) based learning strategies and the scarcity of *in vivo* drug profiles are key challenges hindering the widespread adoption of AI in real new drug development.

Here we presented an approach for functional identification and validation of Central Nervous System (CNS) drug-like compounds by large-scale *in vivo* profiling. A novel microfluidic platform that enabled highly multiplexed screens of hundreds of animals in droplets was proposed. Our system employed air-plugs in the microfluidic chips to capsule the zebrafish larvae in the droplets and enabled the *in vivo* high-throughput screening of drugs. Specifically, large-scale aqueous droplets surrounded by the air phase served as independent reaction vessels. This technique was straightforward, gel-free, and efficient in the process compared to our previously reported agarose-based systems[9]. Furthermore, coupled with an encoded drug loading strategy, our system allows clear identification of all readout signals to particular drugs and combinations. Importantly, we showed that the unique properties of this microfluidic platform enabled unprecedented means to fully screen the drug responses in zebrafish larvae, including their behavioral, cardiac, and neuronal activities, which were not technically feasible previously due to their small size, fragility, and spontaneous behavioral activities. To validate the functionality of our system, we temporally recorded the whole-brain activities of thousands of animals, resulting in the dataset comprising 10,000,000 brain images of zebrafish larvae including 1,000 drug conditions. Coupled with machine learning strategies, a functional classifier for anti-Parkinson-like drugs was also constructed based on the brain activity phenotypes. Notably, we provided a novel foundation to identify anti-

Parkinson-like drug leads, which have been successfully validated in the animal disease models in this proof-of-concept study. Several identified drug candidates including linezolid, cladribine, meropenem, capecitabine, lomefloxacin, and matrine paired with bulleyaconitine A, showed varying degrees of improvement in toxin-induced locomotor deficits, accompanied by attenuation of reductions in dopaminergic neuronal reporter signals in different Parkinsonian animals. To the best of our knowledge, it was the first time to show a fully integrated approach to performing high-throughput *in vivo* profiling and functional validations of drugs. We envisioned that our foundation could contribute to finding optimal medications for brain diseases and was ready to be modified to enable large-scale sequential mono/polytherapy screening for other specific complex disorders, e.g., cancers.

Results

Framework for in vivo identification and validation by microfluidic manipulation and machine learning

As schematically illustrated in Fig. 1, the proposed large-scale *in vivo* profiling platform consisted of four key modules. First, using the transgenic zebrafish line Tg(*elavl3: H2B-GCaMP6f*) with a genetically encoded calcium indicator, a fully automated *in vivo* screening system combining droplet microfluidics and computer vision-based control methods was developed to monitor drug-induced physiological responses in thousands of transgenic zebrafish larvae exposed to 1,000 pharmacologically active drug conditions (**Supplementary Figure S1**). Using rigorous high-throughput methodologies with a particular focus on brain activity phenotypes, we collected time-series fluorescence images of neuronal activity patterns that formed the foundational dataset for subsequent analysis (Fig. 1a). Furthermore, we developed an innovative machine learning model, CNS Drug-like Prediction (CNSDIP) **(**Fig. 1b**)**. The model architecture first applied Principal Component Analysis (PCA) to the image sequences to extract the top 20 principal components (accounting for the highest variance) as feature vectors for downstream computation. These optimized features were then used to build the functional classifier by combining consensus clustering strategy and hypergeometric tests. Further coupling with a Random Forest algorithm, a pharmacological prediction model for classifying and ranking the anti-Parkinson-like drugs was developed. The trained CNSDIP model was then applied to identify the drug conditions (Fig. 1c). Leveraging the functional validation capacity of our platform, various endpoints including bio-toxic, physiological, and behavioral readouts from the top-ranked drug candidates were further collected to validate their hypothesized anti-Parkinsonian effects in 1-methyl-4-phenyl-1,2,3,6-tetrahydropyridine (MPTP)-induced disease animal models (Fig. 1d). This integrated framework provided a systematic approach for monitoring multidimensional organismal responses to pharmacological interventions, potentially leading to identification of new drug/drug pair candidates.

Design of the FD system

To enable high-throughput multiplexed screens using zebrafish, we developed a fully integrated fish-in-droplet (FD) system, evolving from the droplet-based microfluidic technology and automated animal immobilization technique, to generate independent containers for efficient encapsulation of single

animals, which could be further utilized to facilitate a broad range of chemical, analytical, and biological applications (Fig. 2a). To allow multiplexed *in vivo* screens, several microfluidic devices (trapping chip I to III) were designed and fabricated with specific trapping modes to immobilize zebrafish larvae with targeted orientations or free mobility in the droplets (Fig. 2b-d). Unlike the traditional gel-based zebrafish larvae immobilization methods or our recently developed hydrodynamic force-based techniques, no continuous fluidics, anaesthetization, or tedious gelling manipulation was required during multi-organ imaging in our FD system[6, 16, 17]. To allow large-scale screening in practical applications, 15 × 6 array devices were also designed and fabricated by high-precision computer-numerical control (CNC) machining and polydimethylsiloxane (PDMS) demolding in this study (Fig. 2e-g, **Supplementary Figure S2&S3**).

To automatically generate large-scale FDs before immobilization in trapping chips, a microfluidic device with a T-junction geometry was designed and fabricated (Fig. 3a). Unlike the conventional oil-based droplet systems used in *in vitro* assays, the gas (air) was engaged as the continuous phase to generate discrete and uniform aqueous droplets (Fig. 3b). The gas-liquid droplet microfluidic systems maintained a higher surface tension than the liquid-liquid one as shown in **Supplementary Figure S4**. Such surface tension well confined the animal in a droplet to maintain a stable FD (**Supplementary Movie S1**). The automated loading, transportation, and encapsulation of the larvae were facilitated by a home-made handling system, which was similar to our previously reported platform that integrated digitally controlled syringe pumps, microfluidic valves, CMOSs and computer-vision control modules (**Supplementary Figure S5, Supplementary Movie S2**). Efficient single-animal encapsulation and transportation were essential for high-throughput *in vivo* assays. However, it was still challenging due to the animals' size and spontaneous behaviors during handling. To overcome this limitation, a video-detection module, coupled with an in-house developed image processing algorithm, was also developed in our handling system for rapidly detecting zebrafish in a droplet (**Supplementary Figure S6&S7**). **Supplementary Figure S6e** showed the complete process of the automated generation of the zebrafish droplet. In this proof-of-concept study, only ~ 13 minutes were required to generate 100 fish droplets (including 4.6 ± 2.1 seconds per fish droplet for larva loading from the reservoir and 3.7 ± 0.2 seconds/per fish droplet for larva encapsulation in the droplet) in the generating chip (**Supplementary Figure S6f**). Our test results showed that the flow rates of E3 water, drugs, and air in all the inlets were controlled respectively to ensure an adequate droplet-to-droplet spacing, which was crucial to ensure further high precision of drug injection and robust operations (**Supplementary Figure S8a&b**). In this study, each fish droplet was generated with volume of 6.70 ± 0.12 μL during large-scale screening.

To massively upscale the additional number of drugs or drug combinations during *in vivo* screening, microfluidic pipelines coupling with digitally controlled syringe pumps and microfluidic valves were employed in the FD system. Similar strategies had been used for the *in vitro* screening of drug combinations on cancer cells from patient biopsies[14, 15]. Each injection channel was relatively smaller (width: 500 μm) than the main channel so that the drugs could be easily squeezed into the FDs (Fig. 3c-f). During injection, owing to the Laplace pressure difference induced by the surface tension between the

injection phase and air phase, a high-curvature meniscus was formed near the outlet of the nozzle to serve as a pressure barrier. Such a pressure barrier was applied to maintain a quasi-static state and enable injection when a droplet passed through (Fig. 3d, **Supplementary Movie S3**). At each injection nozzle, the passing droplet and the drug were separated by a thin layer of air when the respective syringe pump was inactive, which was important to avoid drug cross-contamination (Fig. 3e). As shown in Fig. 3f, drug addition in droplets could be rapidly generated by the microfluidic pipeline in 1 minute.

To identify the FDs belonging to different drug conditions, we introduced a simple barcoding method in this platform (Fig. 3g, **Supplementary Figure S8c&d**). Generally, every single drug injection would be tagged with specific barcodes including colors and volumes. In this proof-of-concept study, various self-defined patterns of food dyes were utilized to encode the droplets, e.g., a plug with a specific color following a droplet was considered as the corresponding drug label (Fig. 3h**&i, Supplementary Movie S4**). Importantly, the volume of the plug was also defined to be linear to the concentration of the injected drug (**Supplementary Figure S9**). The 10-inlet droplet-generating chip system was ready to be employed for combinatorial drug screening, offering a theoretical maximum encoding capacity of 1,023 unique conditions (10 single drugs and 45 pairwise combinations in a single experiment was generated in this study) × n concentration gradients (where n = 3 in our experimental design). Furthermore, the decoding ability was also evaluated via a quantitative analysis. As shown in Fig. 3j, 1,000 images had been converted into strings of RGB value barcodes and droplet volumes, which could be accurately converted back into the initial images (100%) and code IDs (accuracy with droplet volume, 95.0 ± 2.5%; accuracy with RGB value, 98.5 ± 1.5%). Importantly, owing to the hydrophobic barriers of the all-PDMS microfluidic chip, no cross-contamination was detected during drug delivery and fish droplets transportation via employing fluorescein isothiocyanate and fluorescent microscope imaging (Fig. 3k**&l**). Collectively, such a color/volume-on-demand coding strategy enormously increased the coding capacity and versatility of our platform, which was highly valuable for the further high-throughput screening of combinatory drug pairs.

Multiplexed screening using the FD system

As an initial demonstration of the capability to enable multiplexed screens in real-time in response to acute drug treatment, we first quantified the effects of two well-known neural regulatory chemicals, pentylenetetrazole (PTZ) and tricaine (MS222)[16], by monitoring the behaviors and multi-organ of zebrafish larvae using the proposed FD system (Fig. 4a-c, **Supplementary Movie S5**). Generally, using the trapping chip I, it was simple to enable behavioral recording of the freely swimming larvae in the droplets (Fig. 4d). As shown in Fig. 4e**&f**, numerous behavioral responses including pectoral fin beats and tail movements in multiple single animals could be quantitatively assessed. PTZ is a GABA (Gamma-aminobutyric acid) receptor antagonist and is widely used to induce seizures in various animal models including zebrafish. 10 minutes after PTZ treatment, both fin beats and tail movements of the animals were significantly increased (Fig. 4g**&h**). In contrast, MS222, a widely used anesthetic reagent for zebrafish larvae, dramatically reduced the animals' behaviors.

It was worth noting that large-scale transportation, orientation, and immobilization of the zebrafish larvae in droplets were achieved by the proposed microfluidic systems. After being loaded in the microfluidic devices like trapping chip II&III, various specific orientations of the trapped animals could be easily realized by microfluidic structure design and droplet confinement. In this way, most major organ systems including the brain, heart, liver, and vessels could be optically accessed in our system. For example, a dorsal orientation of a single animal in a droplet could be enabled by trapping its tail in a restricted channel with a specifically designed angle (Fig. 4i). Thus, the continuous and quantitative examination of the cardiac function in response to the acute treatment of PTZ and MS222 in zebrafish could be largely simplified in the array as shown in Fig. 4j**&k**.

Besides, using the transgenic line *Tg(elavl3:H2B-GCaMP6f)* that is genetically encoded with a calcium indicator, our technique was ready to be utilized to analyze brain-wide activity in dorsally-oriented larval zebrafish (Fig. 4l). Calcium imaging in multiple focal planes along the ventral direction was performed in this study, which enabled quantitative analysis of the drug-induced fluctuations of brain activities of the animals. The accumulated calcium transient counts were identified from the fluorescence fluctuations of each ventral plane to construct a brain activity map (BAM) for every single larva. Via T-score testing, a T-score BAM unique to each drug was generated from 5 BAMs that were acquired following drug treatment in 5 individual larvae as we demonstrated recently[17]. Compared to the E3 water-treated groups, the T-score BAMs clearly showed that PTZ activated the neurons in almost all the brain regions of the animals while MS222 inhibited the neural firing in the whole brain (Fig. 4m). Taken together, multiplexed assays were successfully demonstrated in our system, which was previously impossible in the existing microfluidic systems.

Biosafety assessment of the FD system

The proposed automated droplet-based encapsulation and immobilization without human interference or temperature fluctuation did not induce any detectable injury to the animals, which was consistent with our further health assessment. To evaluate the biocompatibility of the FD system, we next assessed the health of 250 larvae after running through a complete experimental cycle using different devices in our platform. In a 4-day health assessment, no any injury was detected in the animals that were released from the microfluidic system (**Supplementary Figure S10**). It was noted that the larvae released carefully from the system showed good locomotion behaviors after running through a complete experimental cycle in the FD system, which collectively indicated good biocompatibility of our system. Moreover, to validate the on-chip biocompatibility of our technique, we evaluated the physiological changes of the animals in long-term observation. Compared to the traditional oil-based droplet systems, our system showed a higher survival rate (**Supplementary Figure S11**). As shown in **Supplementary Movie S1**, zebrafish larvae in water/oil systems would frequently escape from the droplets, causing injury to the animals and eventually making them die in the oil phase. Moreover, the air was used as a continuous phase to generate discrete and uniform aqueous droplets in our system. Such water/air systems would provide more oxygen to dissolve into the droplets for the animals in the long-term evaluation compared

to the water/oil system. Importantly, in a continuous 24-hour evaluation, both of the droplet-generating chip (97.5 ± 2.5% survival rate) and the trapping device (97.5 ± 0.3% survival rate) showed excellent biosafety for long-time live imaging (**Supplementary Figure S12**). It was widely accepted that the microenvironment within the droplet, e.g., the oxygen dissolution level, accumulation of metabolites and spatial confinement, played a critical role in the viability of the zebrafish larvae. We therefore performed a systematic evaluation of key water quality parameters within the droplets, including dissolved oxygen (DO), pH, ammonia (NH_3), and lactate, over a 24-hour period (**Supplementary Figure S13a-d**). The results showed that while DO gradually decreased and ammonia levels increased over time, both remained within physiologically tolerable ranges for zebrafish larvae for at least 16 hours in the droplets. pH and lactate levels also showed only minor changes within the 24-hour period. Crucially, these results demonstrated that the microenvironment within the droplets remained stable and non-toxic for zebrafish larvae for a period far exceeding the typical duration of screening experiments (≤ 10 minutes) in this study. Moreover, the droplets generated in our chip were suitable for manipulating larvae ranging from 4 to 7 days post-fertilization (dpf) as shown in **Supplementary Figure S13e**. Collectively, it suggested that our air-liquid droplet microfluidic system offered the capability of large-scale manipulation of the living animals in a safe way, which could benefit the subsequent *in vivo* screening.

Large-scale in vivo profiling of drugs

This section described the large-scale *in vivo* profiling of drugs including drug exposure and whole-brain physiological recording in step 1 as shown in Fig. 1a. Driven by the urgent need for high-throughput neurological drug screening in animal models, and leveraging the capacity of our platform for multiplexed *in vivo* profiling in zebrafish, we applied our FD system to screen a compound library (Fig. 5a). Following screening of 1,000 drug conditions, including 940 single-drug conditions and 60 drug combinations, the drug-induced changes in whole-brain activities were temporally recorded via calcium imaging using the trapping chip II. This resulted in a raw dataset (over 23 TB in size) that comprises more than 10,000,000 original images.

This section described the CNSDIP model development and training in step 2 as shown in Fig. 1b. Via quantitative analysis and T-score testing of calcium fluctuations, thousands of T-score BAMs were generated. In this proof-of-concept study, the T-score BAMs of 11 clinically used anti-Parkinson drugs that we screened previously, including a variety of known molecular targets including dopamine agonists, anticholinergic agents, monoamine oxidase inhibitors, and catechol-o-methyltransferase inhibitors, were randomly selected and utilized in further large-scale functional identification of anti-Parkinson-like (N04-like) candidates or possible symptomatic treatment leads[17]. To extract the intrinsic coherence among these T-score BAMs, a two-step machine learning- based approach was utilized in our CNSDIP algorithm. First, the dimensionality and noise of the BAMs were reduced via principal component analysis (PCA). In this screen, the top 20 principal components (PCs) were selected to describe the major pattern variation (> 57%) across all T-score BAMs (**Supplementary Figure S14**). Second, consensus clustering, an unsupervised classification approach, was employed to dissect the

phenotypic diversity of the T-score BAMs using the 20 PCs (**Supplementary Figure S15)**. In this study, 7 clusters were identified in a blinded fashion (Fig. 5b).

This section described the prediction and prioritization of the drug candidates in step 3 as shown in Fig. 1c. To further confirm the anti-Parkinson drug-like classifier, a hypergeometric test was employed in our CNSDIP platform for statistical analysis of the link between our T-score BAMs based clusters and the specific therapeutic categories as determined by the World Health Organization (WHO) Anatomical Therapeutic Chemical (ATC) classification system. As shown in **Supplementary Figure S16**, T-score BAMs based Cluster 4 was found to have a strong association with the N04: Anti-Parkinson Drugs ATC category ($p < 0.05$, hypergeometric tests), with a subgroup of 6 clinically used anti-Parkinson drugs within the cluster. As visualized in the 20-dimensional space and T-score BAMs, the in-cluster drug conditions and the anti-Parkinson drugs showing similar features suggested modulating effects in specific brain regions including dopaminergic systems (Fig. 5c-f). For example, we observed that the U.S. Food and Drug Administration (FDA) approved Parkinson's therapies—the monoamine oxidases (MAO) inhibitor rasagiline, the anticholinergic benzhexol, and the catechol-O-methyltransferase (COMT) inhibitor entacapone—all robustly increased neural activity in multiple larval brain regions, including the telencephalon, pretectum, paraventricular organ, locus coeruleus, midbrain-hindbrain boundary, raphe nuclei, and reticular formation (Fig. 5d**&e**). Notably, similar upregulation effects were also found in the identified drug conditions, e.g., cimetidine, capecitabine, linezolid, irbesartan and fenbufen (Fig. 5f). Moreover, these results also showed that repeated control conditions (DMSO groups) remained quite constant throughout the entire screen, further confirming that the neuronal physiology of animals in droplets was consistent over time, and that partial immobilization of the larvae in the on-chip droplets did not affect the viability of the animals (**Supplementary Figure S17&S18**).

After identification of the anti-Parkinson drug-like classifier, the in-cluster drug conditions were further prioritized via a Random Forest classifier based ranking system (Fig. 5g). Basically, the Random Forest-based CNS classifier built in the CNSDIP model was trained by a small T-score BAM dataset containing 363 drugs (180 clinically-used CNS drugs and 183 non-CNS drugs). During the further test of 600 drugs, a prediction accuracy of 84% was achieved in such a CNS classifier (**Supplementary Figure S19**). Collectively, this model generated CNS prediction probabilities for each in-cluster T-score BAM, which was then used as a quantitative index to rank the final therapeutic potential of the identified anti-Parkinson-like drug conditions. It was encouraging that several top-ranked compounds had been previously demonstrated to have neuroactive effects *in vitro* and *in vivo*[18]. For instance, ferulic acid, a phenolic compound commonly used in traditional Chinese medicines, had been shown to confer neuroprotective effects against Parkinson's disease, attributable to its potent anti-inflammatory and antioxidant properties[18]. Besides, telmisartan (an angiotensin type 1 receptor antagonist), matrine (a natural alkaloid) and palmatine (a protoberberine alkaloid) had also been reported to ameliorate the motor deficits in Parkinsonian rodents[19–21]. Notably, these reports partially supported the functionality of our FD system and CNSDIP model as an effective anti-Parkinson drugs screening platform.

Validation of the anti-Parkinson-like candidates

This section described the independent *in vivo* validation of the top-ranked drug candidates in step 4 as shown in Fig. 1d. To further validate the results of the machine learning-based CNSDIP model, we selected the 16 top-ranked anti-Parkinson-like candidates for functionality and biosafety tests. The candidates tested here were selected by CNSDIP solely based on brain-activity similarity. And several independent validation experiments were performed in this study. Notably, these validation assays were designed to comprehensively assess the therapeutic potential of candidate compounds, rather than retroactively benchmarking our system as a neuroprotection predictor. Here, two experimental paradigms, including co-treatment and post-treatment, were adopted (Fig. 6a). As demonstrated in **Supplementary Figure S20**, although all identified drug conditions showed no healthcare impact on the larvae in our initial screen, 5 drug conditions were found to be toxic during a long-term assay in droplets. Then a behavioral test was performed using three different zebrafish Parkinsonian models (1-methyl-4-phenyl-1,2,3,6-tetrahydropyridine (MPTP)-induced, Rotenone-induced and 6-hydroxydopamine (6-OHDA)-induced) in the FD system using the trapping chip I (Fig. 6b). MPTP, 6-OHDA, and Rotenone were widely used neurotoxins to induce Parkinsonism models across a wide range of vertebrates, including zebrafish[22, 23]. MPTP, via its metabolite MPP+, was reported to inhibit mitochondrial complex I and reliably induce dopaminergic neuron loss and locomotor deficits in both larval and adult zebrafish[24, 25]. 6-OHDA was shown to cross the blood-brain barrier more readily in zebrafish than in rodents, leading to widespread oxidative stress and dopaminergic neuron reduction[26]. Rotenone was also a high-affinity inhibitor of mitochondrial complex I that induces both motor and non-motor symptoms in zebrafish following chronic low-dose exposure[27]. By specifically perturbing the dopaminergic system of the zebrafish, these compounds induced behavioral deficits in the animals. As shown in Fig. 6b**&c**, three Parkinsonism models that employed in this study all showed significant inhibition of the freely moving behaviors of zebrafish larvae in the FDs. Compared to the control group, a pronounced reduction of the moving scopes (21.6 ± 7.7% in MPTP group, 16.8 ± 6.0% in Rotenone group and 18.6 ± 7.1% in 6-OHDA group) and numbers (7.7 ± 3.7% in MPTP group, 2.8 ± 0.9% in Rotenone group and 9.2 ± 3.8% in 6-OHDA group) was observed, which further confirmed the successful establishment of Parkinsonism models (Fig. 6d**&e**). In this study, following a 72-hour drug co-treatment period or a 24-hour drug post-treatment, the locomotion behaviors of the MPTP-induced Parkinsonian zebrafish larvae were monitored for 10 minutes. The results confirmed again that several candidates showed side effects including teratogenic toxicity and lethal toxicity (Fig. 6f**&g, Supplementary Figure S21-23**). After excluding the candidates with long-term toxicity, 5 compounds and 1 compound pair showed a significant recovery of the moving times compared to the Parkinsonism model groups (Fig. 6f, **Supplementary Figure S21**). In addition, the behavioral deficits effect in behavioral scopes was also reversed by typical drugs/pairs in this test (Fig. 6g, **Supplementary Figure S21**). Interestingly, although several of the identified candidates had previously demonstrated a certain degree of neuroprotective effects, most had not yet been specifically investigated for potential anti-Parkinson's functionalities. For example, linezolid, an antibiotic used for the treatment of infections, recovered the locomotion behaviors of the Parkinsonian animals without any observable morphological effect in both treating modes (Fig. 6h**&I**). As linezolid's MAO inhibitor activity

had been previously reported, the observation that linezolid exhibited protective activity in our assay is well consistent with its established mechanism of action[28–30]. Another antibiotic, meropenem[31], was also found to recover the behavioral deficits in Parkinsonism model groups with a post-treatment mode (Fig. 6i**&m**). Moreover, a purine analogue (cladribine) used to treat leukemia[32], and a drug combination, matrine (1 μM) paired with bulleyaconitine A (1 μM), were also validated to improve motor impairments in Parkinsonian animals with a co-treatment mode (Fig. 6j-k, o-p). Taken together, these observations in the zebrafish Parkinsonism model further showed a promising symptomatic effect of the drug conditions identified by the proposed FD system and CNSDIP model.

Leveraging our FD platform's capability for high-resolution fluorescence imaging of specific organs and cell clusters, we further primarily evaluated the cellular effects of the candidate compounds on dopaminergic (DA) neurons *in vivo* using confocal imaging (Fig. 7a). It was commonly accepted that the progressive loss of DA neurons in the affected brain areas was one of the pathological features of Parkinson's disease[33]. And the complete development of the dopaminergic system in zebrafish larvae within 5 days post-fertilization (dpf) facilitated their use as a suitable model for the rapid *in vivo* evaluation of chemical-induced DA neurotoxicity[34]. Hence, using the transgenic line *ET(vmat2:GFP)* with green fluorescent protein (*GFP*)-labeled dopamine neurons, we quantitatively assessed the ability of the candidate compounds to attenuate neurotoxin-induced neurochemical phenotypes in dopaminergic neurons across various Parkinsonism models using confocal imaging[35]. Given that DA neurons of the zebrafish posterior tuberculum (PT) have been suggested to be anatomically and physiologically homologous to mammalian nigrostriatal dopaminergic projections implicated in Parkinson's disease[36–38], we performed quantitative cell counting of GFP-labeled diencephalic cluster (DC) 2/4 neurons in the PT for functional validation analysis (**Supplementary Figure S24**). The identification of the DC2/4 neurons was based on their anatomical positions, characteristic soma morphology, and relationships to surrounding anatomical landmarks (Fig. 7b). Since toxicant exposure might modify tissue architecture and interfere with the identification of DC2/4 neurons, we performed whole-brain morphological assessments with MPTP as a prototypical toxicant. No significant structural changes were observed, which further supported reliable quantitative comparisons of DC2/4 neurons (**Supplementary Figure S25**). Furthermore, we found that prolonged toxin exposure reduced the number of identifiable DC2/4 cells. Within this identifiable subset, cell counts were lower in MPTP-treated groups relative to controls, consistent with a loss of dopaminergic phenotype rather than reduced somatic area or GFP intensity. As shown in Fig. 7c, apparent reduction of the number of the identifiable DC2/4 neurons could also be clearly observed in other neurotoxin-treated Parkinsonism model groups compared to the control groups. Quantitative analyses also revealed that MPTP, Rotenone, and 6-OHDA treatment induced the reduction of the number of the identifiable DC2/4 neurons in the PT regions (Fig. 7d**-f**). It should be noted that the loss of fluorescence may reflect either loss of dopaminergic neuronal phenotype or true neuronal degeneration, and cannot be exclusively interpreted as irreversible cell death. Importantly, most of the behaviorally validated drug conditions, significantly preserved dopaminergic phenotype in DC2/4 neuron. For example, the numbers of GFP-labeled DC2/4 neurons in animals with co-treatment of linezolid and the paired condition (matrine paired with bulleyaconitine A) were found to be significantly

increased (12.0 ± 1.4 and 13.0 ± 1.3 in the MPTP group, 11.4 ± 1.0 and 10.6 ± 0.8 in the Rotenone group, 10.8 ± 0.4 and 11.6 ± 0.5 in the 6-OHDA group, respectively), compared to the Parkinsonism model groups (6.6 ± 0.2 in MPTP group, 5.4 ± 0.5 in Rotenone group, 6.8 ± 0.6 in 6-OHDA group, respectively). Indeed, not all candidates yielded favorable positive responses in all Parkinsonism models. For instance, capecitabine showed a modest, statistically nonsignificant increase in GFP-positive DC2/4 cell counts in the rotenone model compared with the corresponding toxin-only group. (Fig. 7d-f). Moreover, the co-treatment of cladribine and the post-treatment of the paired condition only attenuated the toxin-induced reduction in dopaminergic reporter signal in MPTP-induced models, with no statistically significant differences observed in other models. It should be noted that almost all the finally identified candidates have never been demonstrated to have any symptomatic or cellular effect. Collectively, these results supported that our droplets-based microfluidic technology and the coupled CNSDIP model could be utilized as a powerful physiology-based screening and functional validation tool for anti-Parkinson drug discovery.

Discussion

To enable organ-specific imaging of vertebrates, traditional evaluation technology required manual agarose mounting with anaesthetization, which was laborious and time-consuming for large-scale screening[39,40]. Even though the development of gel-based capsuling microfluidic systems had enabled automatic handling of the larvae and large-scale drug screening, such techniques usually required complex system setup and pre-screening operations[9]. Moreover, multiplex profiling of the animals including organ-specific evaluations and behavioral monitoring for drug screening was prohibited in the previous platforms. Recent advances in droplet-based microfluidic technology have enabled large-scale drug screening using cell specimens[14, 15]. And several studies have successfully demonstrated that multiphase droplet microfluidics could be applied in high-throughput measurements of multicellular organisms including spheroids and organoids[15,41–45]. However, limited success has been achieved in *in vivo* profiling of drugs, primarily due to the complexity and difficulty in automated immobilization, orientation, and evaluation of the animals in the droplets. Here, we described a high-throughput strategy for *in vivo* multiplex profiling, by using the droplets-based system. Specifically, based on the gas-liquid droplet encapsulation and the unique design of the microfluidic trapping device, our FD system made it straightforward for animal manipulation, orientation, and transportation. To our best knowledge, this was the first reported technique that enabled long-term monitoring of oriented zebrafish larvae in a gel-free, anesthetics-free, and pump-free way. Moreover, a coding strategy was implemented in our platform to enable the large-scale generation of droplets with encoded drug pairs and single animal, which was also highly valuable for high-throughput screening of drug conditions. While our current system could theoretically generate a vast array of distinct drug conditions, in practice, the number of achievable conditions should be jointly determined by several parameters, including the design of the generating chip (e.g., channel length), the barcode sequence length, the minimum single-injection volume of the syringe pump, and the fluidic limitations. It should also be noted that the limited coding capacity would be one of the disadvantages of our method when compared to the binary barcoding scheme. However,

the simplicity and low-cost aspects of our strategy made it a useful supplement tool for barcoding. Moreover, the decoding in this study was based on a commercial tiny camera coupling with a home-developed reading user interface, which could be much simpler than the previously reported fluorescent imaging-based coding strategy[14, 15, 46].

In this proof-of-concept study, imaging orientations of the animals were selectively tuned by different microfluidic trapping strategies to achieve multiplex profiling of the animals. Automated capsulation of the zebrafish larvae with dorsal or lateral orientation was successfully demonstrated using our platform, which offered us the capability to evaluate specific organ systems including the brain, heart and vessels. Importantly, our system had enabled a large-scale generation of microdroplets with single-oriented animal in a gel-free way, which was challenging for previous animal immobilization technologies. Particularly, without agarose mounting and anesthetic treatment, this technique was highly suitable for multiplex profiling using zebrafish, which was also burdensome for other proposed systems. These properties provided great flexibility for *in vivo* assays that required specific imaging angles or multiple phenotyping.

Using this fully integrated microfluidic system, whole-organism-based functional screening and validation of the drug combinations were successfully demonstrated. Importantly, a machine learning-based CNSDIP model was developed to identify compounds exhibiting brain-activity patterns similar to those associated with clinically used anti-Parkinsonian drugs. And these compounds were further prioritized as potential anti-Parkinson-like functional candidates or possible symptomatic treatment leads in this study. It was exciting that several top-ranked drug conditions were identified solely based on the robust neural modulation without any prior chemical or molecular knowledge of the compounds. Collectively, the CNSDIP model provided candidate prioritization based on the brain-activity similarity in healthy animals. To further test the biological effects in toxin models, the behavioral and cellular evaluation were performed independently. Notably, these two stages were sequential, not predictive.

After excluding four drug conditions showing long-term toxicity, 6 of the 12 identified drug conditions (50%) were found to significantly recover the behavioral deficits and effectively alleviate the reductions of GFP-labeled DC2/4 neurons in Parkinsonism models. Importantly, these identified drug conditions did not induce any apparent effect on locomotive behavior in zebrafish larvae without MPTP/Rotenone/6-OHDA treatments (**Supplementary Figure S26**). It further verified that these identified candidates did not simply enhance motor activity in the animals. However, the fact that other drug conditions tested were negative in the Parkinsonian animals might reflect limited sensitivity of the employed Parkinsonism models to detect anti-Parkinson activities mediated through different pathways rather than true lack of efficacy as potential anti-Parkinson agents[25, 47]. Moreover, in most experimental conditions, co-treatment tended to attenuate toxin-associated reductions in dopaminergic reporter-positive cell counts to a greater extent than post-treatment. Importantly, in the post-treatment scheme, candidates were introduced after 48 hours of toxin exposure while the toxin challenge continued. Thus, this scheme assessed drug effects during ongoing toxin exposure rather than recovery from an established, irreversible neuronal lesion. In addition, toxin-associated reductions in GFP-positive cells were also

observed in pretectal neural cluster (Pt) and raphe nuclei (Ra) regions. And several drug conditions including linezolid and the paired condition (matrine paired with bulleyaconitine A), were also found to significantly attenuate such reductions. While alterations in these cell counts represented an interesting observation, further work was necessary to define the biological significance and underlying mechanisms driving this phenomenon. Notably, although various studies have demonstrated that the exposure of neurotoxins, e.g. MPTP, 6-OHDA, and Rotenone, induced neuron loss in specific regions, our current validation approach cannot definitively distinguish genuine neuronal cell loss from specific downregulation of fluorescent reporter signals due to inherent technical limitations[22, 23]. Therefore, while these experiments provided additional biological characterization of the prioritized candidates in zebrafish models of Parkinsonism, the observed cellular effects did not establish neuroprotection, and none of the identified candidates could be classified as a neuroprotective agent based on the present evidence. To better validate the function of the drug conditions and to understand their precise mechanisms, thorough studies using other Parkinsonian animals, larger animal models and in-depth histological analyses would be required. Nevertheless, we envision that our platform opens the way for comprehensive *in vivo* screens of mono/polytherapy for Parkinson's disease treatments that have so far been restricted to *in vitro* assays.

Here, we integrated microfluidics, *in vivo* phenotyping, and machine learning to establish a scalable, automated, and intelligent platform for modern drug screening. Apart from using it for anti-Parkinson drug discovery, our microfluidic platform should also be of interest for further applications, such as identifying other neuroactive drugs including antiepileptics and antidepressants, *in vivo* large-scale sequential treatment assays for cancers[48], high-throughput gene-modulators screening[49] and the exploration of personalized drugs[50]. Moreover, the microfluidic-based animal manipulation, chemical delivery and multiplexed evaluation techniques we demonstrated with our platform could be readily adapted for large-scale screens in other organisms, e.g., *C. elegans*[51] and Drosophila[52]. Thus, we believed that such a feasible and easy-to-build system would be more accessible to researchers in a wide range of fields, and could accelerate the pace of drug discovery.

Materials and Methods

Zebrafish line

The AB strain wild-type zebrafish and the transgenic zebrafish line *Tg(elavl3:H2B-GCaMP6f)*, *Kdrl1:eGFP*, *Gata1:dsRed*, *Cmlc2:eGFP* and *ET(vmat2:GFP)* were maintained in aquaria under standard laboratory conditions (at 28℃ under a cycle of 14 hours light, 10 hours dark). Specifically, the transgenic zebrafish lines *Tg(elavl3:H2B-GCaMP6f)* and *ET(vmat2:GFP)* used in this study were both in the nacre background[35,53,54]. Larvae of 5 dpf were used in the combinatorial drug screening experiments. All animal work was carried out with prior approval from the animal ethical committee of Sun Yat-sen University and was in accordance with local animal care guidelines.

Microfluidic chip

In order to rapidly encapsulate and immobilize non-anesthetized zebrafish larvae in a simple and highly parallel manner for multi-physiological imaging, we developed a microfluidic system for high-throughput immobilizing and trapping animals in the droplets. The key components of the proposed system consisted of two microfluidic chips, the droplet-generating chip and the trapping chip. The droplet-generating chip (Fig. 3a) was designed with S-curve main fluidic channels (1 mm wide and 1.2 mm high) to generate and transport zebrafish droplets sequentially on a large scale. It was also used to enable drug loading and barcoding via injection channels (width: 500 μm).

The trapping chips I to III were designed to allow the orientation and immobilization of zebrafish in droplets for further microscopic imaging. The trapping chip I was designed to immobilize every single fish-droplet in a channel with opened inlet and outlet for allowing behavioral recording of the animals (Fig. 2e). The trapping chip II&III with an array of trapping channels and structures was designed to trap larvae on a large scale with a dorsal or lateral orientation (Fig. 2f**&g**). The zebrafish were loaded with a specific direction (heads facing forward) into the trapping channel via an automated droplets-loading system. A tapering design with a narrow restricted portion (150 μm) in each trapping channel, which only fitted the tail of a larva, was particularly important for robust immobilization and orientation of the animal. This structure also protected the animals from injury.

As shown in **Supplementary Figure S3**, the convex molds for the droplet-generating chip and the trapping chip were milled by a high-precision computer-numerical-controlled machine (CNC, Dingsheng CNC Equipment Co., Ltd.) using a copper plate. **Supplementary Figure S2** showed the complete procedures for the fabrication of microfluidic devices in this study. After machining, the molds were cleaned with 100% alcohol overnight and rinsed a couple of times. The polydimethylsiloxane (PDMS) was then poured onto the convex mold. After completely removing the air bubbles in a vacuum chamber, the mold with a PDMS layer was baked in an 80℃ oven for 4–6 hours. Then the cured PDMS layer was demolded for further punching to form the inlets and outlets. At last, the plasma treatment (Shenzhen Sanhe Boda Electromechanical Technology Co., Ltd.) was carried out to temporarily bond the microfluidic layer to the glass substrate to make the final microfluidic chips used in this study.

Automated generation, transportation and dispensing of zebrafish droplets

The automated generation, transportation and deposition of droplets containing single zebrafish larva were enabled by a home-made motorized system based on a control board based on STM32F103RCT6 coupling with two CMOS cameras (MT9P031, Onsemi), 5 microfluidic pumps (THBP01, ZHANSUI) and 9 microfluidic valves (WK01, WOKUN Technology) (**Supplementary Figure S5**). First, the zebrafish droplets were generated and collected from the droplet-generating chip. Specifically, the loading and dispensing nozzles were mounted on a motorized X-Y-Z stage in this system. The generating channel was initially filled with E3 water solution via the water inlet/outlet (I/O). And the larva was loaded via an air bubble-

aided module under negative pressure when the zebrafish inlet was opened (**Supplementary Figure S6a**). **Supplementary Figure S6e** showed the complete process of the automated generation of the zebrafish droplet. Upon successful entry of the zebrafish larva into the generating chip, the event was immediately detected by CMOS-based monitoring, triggering a switch in the fluidic path to transport the larva. Once the larva entered the generating channel, the air inlet-initiated air injection. The resulting shear force promoted the formation of a standardized fish-in-droplet unit (6.70 ± 0.12 μL), with a regular volume matching that of the generating channel. This droplet was then delivered into the subsequent serpentine channels for further processing. Second, based on optical sensing signals, the system would identify the direction of the larva in the droplet and actuate the corresponding pumps and valves to ensure the zebrafish droplet was transported with their tails forward (**Supplementary Figure S6b&c**). When the larva's direction was correct (tail-forwarded), valve 2 and valve 5 would be opened, allowing the syringe pump to immediately load the droplet into the trapping chip. If the larva's direction was incorrect (head-forwarded), valve 2 and valve 4 would be opened instead, directing the droplet into a bypass channel; thereafter, the valve 3 and valve 5 would be opened to subsequently load the droplet into the trapping chip with a reversed direction. The dispensation of droplets onto the trapping chip was enabled by computer-controlled syringe pumps and motorized X-Y-Z stage (**Supplementary Movie S2**). According to the inlets of the chamber arrays in the trapping chip, an X-Y location of each droplet was precisely defined to enable fully automated droplet transferring and animal trapping with specific orientation for further high-throughput *in vivo* screening.

The control board in this system contained PCBs with four layers of copper foil (**Supplementary Figure S7**). We used glass fiber cloth as a reinforcing material, bonded with epoxy resin and a copper-clad plate (FR-4, JIALICHUANG) to fabricate the PCB. Lead-free low-temperature soldering paste (LF999, KELLY SHUN) was employed to attach various surface-mounted components, including the ARM Cortex-M3 MCU (STM32F103RCT6; STMicroelectronics), DC-DC converter (TPS54302DDCR, Texas Instruments), microstepping motor driver (A4988SETTRT, Allegro), Low Drop Regulator (AMS1117, Puolop), N-Channel MOSFETs (AO3400A, Born), along with various surface-mount resistors, capacitors, and diodes by heating at 230°C.

The coupled driving software consisted of two primary parts: (i) the OpenCV-based computer-vision program and (ii) the embedded software tailored for the MCU. The computer-vision program was developed in Python, which was capable of issuing control commands to the control board and the motorized X-Y-Z stage through a UART port while processing visual tasks, enabling the system to achieve closed-loop control based on visual feedback. Its design consisted of two parts. First, the visual detection in the loading module: after simple filtering and binarization processing of the image obtained by Camera 1, it could quickly determine whether there was a zebrafish larva in the field of view of Camera 1, allowing the system to capture the appropriate time for transportation. Second, in the process of regulating the direction of the zebrafish: After performing morphological processing such as median filtering, binarization, erosion, and dilation on the images captured by Camera 2, the eyes of the zebrafish, as important features, could be accurately segmented, enabling coordinate tracking. Furthermore, in combination with the algorithm for gray scale comparison, the direction of the zebrafish

could be accurately distinguished, which was then used to enable coordinate tracking and corresponding control commands sending (**Supplementary Figure S6**). A customized firmware was developed for the STM32F103RCT6 microcontroller using the C language and the standard peripheral library. This firmware enabled the control board to execute commands received via UART port from a host computer, coordinating the operation of pumps and microfluidic valves. To ensure real-time performance, control sequences for these components were pre-packaged into efficient routines. The system supported multiple operational modes, facilitating precise, on-demand fluidic control through stepper-motor-driven pumps and valves.

Compound additions in zebrafish droplets

For the addition of compounds into the micro-droplets containing zebrafish, the squeezing method reported recently was applied in this study[55]. Initially, the droplets generated at the entrance of the main channel were transported to the U-corner of the microfluidic system for adding single and combination compounds (**Supplementary Movie S3**). The compound addition inlets were relatively small so that the compounds could be squeezed into the droplets at the U-corner by actuating the corresponding pumps to facilitate compound injection. Via sequential injection of chemical fluids through the inlets at the flowing speed of 25 μL/min, droplets containing compound combinations were finally formed in a large-scale for further physiological evaluation in this study. Particularly, a thin layer of air was employed to separate the passing zebrafish droplets from the injection compounds at the injection nozzle during the inactivation situation, which made the drug additions without any cross-contamination.

Compound barcoding

The barcoding strategy relied on the number and volume of the barcoded microdroplets to distinguish the categories and concentrations of the compound combinations (**Supplementary Movie S4**). The different color dyes correlated with different compounds, and the volumes of each microdroplet represented specific concentrations used in the assays. The idea was realized by coupling with the S-shaped microfluidic chip, with the left inlets of the microfluidic chip set as the compound injection inlets and the right inlets set as the coding droplet inlets. After adding the compound to the zebrafish droplet, a microdroplet containing a specific volume of the corresponding dye solution was generated following the zebrafish droplet as its barcode. Then the barcodes behind the zebrafish droplet quickly revealed detailed information about the added compounds.

Health assessment

To assess the health status of larvae processed by the FD system, all larvae were immobilized in the droplets. Their health was monitored in the following 48 h. The criteria for health assessment included both functional and morphological abnormalities. Functional criteria included visual confirmation of normal heartbeat and blood flow rates. Morphological criteria included spine bending (i.e., lordosis, kyphosis, and scoliosis) and craniofacial abnormalities. To minimize this biological source of variation, we used larvae from a single, high-quality clutch for all replicates. Importantly, to further minimize

evaporation and stabilize osmotic conditions, a home-made wet chamber was also employed in this study to maintain constant humidity around the droplets.

Aquatic environment assessment

To systematically evaluate the aquatic environments within the droplets, the dissolved oxygen (DO), pH, ammonia (NH_3), and lactate levels were monitored over a 24-hour period in this study (**Supplementary Figure S13a-d**). Briefly, DO, ammonia, and pH were measured using commercial electrochemical sensors, including AR8010 (XIMA) for DO, SN-3004-NHN-N01-10 (VEMSEE) for ammonia, and SN-3003-PH-N01-201T (VEMSEE) for pH. The lactate concentration was quantified using a commercial L-lactate dehydrogenase (L-LDH) activity assay kit (BC0685, Solarbio). To enable reliable measurement at each time point, 224 individually cultured fish droplets were pooled together to achieve a sufficient sample volume (1500 μL) for tests using commercial sensors or assay kits. All the aquatic environment assessments were repeated with 10 independent biological replicates. To avoid evaporation of the droplets in the FD system during long-term evaluation, a homemade wet chamber was also adapted to the testing stage to keep a relatively humid environment at a constant temperature (28°C).

Concentration validation

An ultraviolet-visible micro-spectrophotometer (K5800C, Beijing Kaiao Technology Development Co., Ltd.) was used to validate the final concentrations of the solutions of methylene blue based on the proportional relationship between the ultraviolet absorbance and solution concentration (**Supplementary Figure S9**). Samples with five concentrations of 1 μM, 5 μM, 10 μM, 20 μM and 30 μM were prepared for the determination of the molar absorptivity of the methylene blue. This molar absorptivity curve was then used to determine the final concentration of the diffused solutions in the droplets in this study.

Compound library and chemical treatment

We screened a library of structurally-diverse compounds (**Supplementary Figure S1)**. All compounds were dissolved in DMSO as a vehicle as ~ 10 mM stock solutions. Three final concentrations (1 μM, 10 μM and 100 μM) of compounds were mainly tested in the primary screen. And 10 μM, a commonly used concentration in larval zebrafish-based drug screen, was selected to test in most part of this study[56]. In the validation tests, the concentration of compounds was selected based on the clustering results of their brain activity maps. All the chemical compounds were purchased from Topscience Co. Ltd.

Microscopy

Imaging was performed on a fully automated inverted fluorescent microscope (Leica THUNDER DMi8) equipped with a cooled high-speed sCMOS camera (DFC 9000GT) and a 10X (NA, 0.4) objective. LAS X software was installed to control the microscope. When performing epifluorescence microscopic imaging of the brain activities, the camera was operated at a 10 Hz frame rate with 50 ms exposure time to ensure that necessary information was captured. When performing microscopic imaging of the cardiac and behavioral activities, the camera was operated at a 10 Hz frame rate with 1 ms exposure time. For confocal imaging, NIKON AX microscope with a resonant scanner was used. The NIS-Elements

software was installed on the device for overall image acquisition. Confocal microscopy was only used to enable cell counting in the validation tests, which were shown in Fig. 7.

Heartbeat analysis

Cardiac signals before and after different drug treatments in each larva were recorded. Using the software ImageJ, the heartbeat signals were manually extracted via calculating the changes of pixel values in the ROI (Region of Interest) resulting from the contraction-relaxation cycle of the heartbeat (Fig. 4i). In the further cardiac analysis, the envelopes and peaks were extracted from the raw data using specific functions in Matlab, including Filters and Findpeaks. The low frequency (< 0.2 Hz) noise was filtered by a Highpass Butterworth Filter. Then the peaks of the signal were extracted and counted, which was used to finally plot the corresponding heart rate variation curve to different drug conditions.

Behavioral activities analysis

Locomotion behaviors of the animals before and after different drug treatments in each larva were recorded. The plugins “Z-project” and “Multi Kymograph” in software ImageJ were used to analyze the fin and tail movements (Fig. 4e**&f**). Then, the number of changes in ROI pixel values caused by the fin beats/tail movements of the zebrafish were analyzed through Matlab as the number of fin beats and calculate the fin beats/tail movements rate (Fig. 4e**&g**).

Brain-wide activities analysis

The analysis of the brain-wide activity was similar to our previous demonstration[17]. Firstly, in order to map the activation level of the brain, each frame of the calcium imaging was meshed into small ROI with a size of 15 μm^2. Then the calcium transient counts (*c*) of each ROI were calculated by averaging the calcium signal changes:

$$c = \frac{1}{n}\sum_{i=1}^{n-1}(m_{i+1} - m_i)/m_0$$

Where *n* represented the number of images and *m* was the pixel value of the calcium signal of each ROI.

By taking the changes (increase or decrease) in the number of calcium transients in each ROI, a brain activity map (BAM) $M = \left[d_{ij}\right]$ was derived before (t_0) and after chemical treatment (t_1), and summed across multiple layers along the Z-axis:

$$d_{ij} = \sum_k c_{ijk}^{t_1} - c_{ijk}^{t0}$$

where $c_{ijk}^{t_0}$ and $c_{ijk}^{t_1}$ were the calcium transient counts of the ROI at row *i* and column *j* of the *k*th layer before and after chemical treatment, respectively.

Lastly, to quantitatively evaluate the statistical significance of the regulation of brain activities by each compound/compound combination, a heat map describing a matrix of T-scores (T-score BAM),

$T = \left[t_{ij}\right]$ was calculated for each ROI across the five BAMs from different biological replicates by:

$$t_{ij} = \frac{\overline{d_{ij}}}{S_{d_{ij}}/\sqrt{n}}$$

where $\overline{d_{ij}}$ was the mean brain activity score of the ROI at row *i* and column *j* of the five BAMs, $S_{d_{ij}}$ was the standard deviation of the mean, and *n* was the number of biological replicates.

CNS drug-like prediction model

In this study, we established an innovative CNSDIP model that combined principal component analysis (PCA) with the Random Forest algorithm.

Firstly, PCA was applied to all T-score BAM data for dimension reduction and noise filtering. In this study, the top 20 principal components (PCs) were selected to describe the major pattern variation (> 57%) across all T-score BAMs (**Supplementary Figure S14**).

Then, an unsupervised classification method was employed to dissect the phenotypic diversity of the drug conditions based on their T-score BAMs. Consensus clustering based on hierarchical clustering and bootstrap resampling (*n* = 1,000) was performed on the top 20 PCs. Since the area under the empirical cumulative distribution function curve did not increase significantly from 4 clusters to 5 clusters (< 1%), 7 optimal phenotypic T-score BAM clusters were identified (**Supplementary Figure S15**).

To link the identified phenotypic BAM clusters with CNS drug categories in ATC systems, we conducted a hypergeometric overrepresentation test. In the test of overrepresentation of ATC classes in BAM clusters, the hypergeometric *p*-value was calculated as the probability of observing *k* or more ATC class drugs among the total *n* drugs in a specific BAM cluster. For each pair of BAM clusters and ATC categories, the obtained *p* values were used to identify statistically significant associations ($p < 0.05$).

Finally, the top 20 PCs of the BAM data in the identified cluster were further input into the Random Forest-based ranking model. This model employed Random Forest as its core architecture with the specific parameter configurations as follows: *n_estimators* = 28, *random_state* = 10, *max_depth* = 7, *max_leaf_nodes* = 100, *max_features* = 4. This model integrated multiple decision trees and aggregated the prediction results of each tree through voting or mean mechanisms, thereby achieving robust and highly generalized classification performance. During the model training process, each decision tree selectively extracted sample subsets from the training set based on the *bootstrap sampling* method. In addition, only randomly selected 4 features (*max_features* = 4) as candidate splitting attributed for determining the optimal split. This mechanism effectively enhanced the diversity of the model and significantly reduced the risk of overfitting. We trained the model using a dataset containing 363 high-quality BAM samples, and ultimately achieved a prediction accuracy of ~ 80% on the validation set (**Supplementary Figure S19**).

We used the *predict_proba* method to obtain the independent probability prediction results of each decision tree for each category in the Random Forest. The output was the probability distribution of each drug condition being determined as a specific category, and this value reflected the average support ratio of its corresponding category prediction in all decision trees.

$$P_i = \frac{1}{n}\sum_{t=1}^{T} y_i^{(t)}$$

$$y_i^{(t)} = \begin{cases} 1, If\ the\ tree\ predicts\ that\ the\ compound\ belongs\ to\ CNS \\ 0, else \end{cases}$$

.

P_i was the prediction probability, *T* was the number of decision trees, and the prediction result of the *t*-th tree for this compound was $y_i^{(t)}$.

Based on the predicted probabilities output from the model, all the drug conditions were systematically ranked towards therapeutic potential.

Toxicity assay using the FD system

The toxicity of drug candidates was evaluated in a co-culture assay using zebrafish larvae (Danio rerio, wild-type strain). Fertilized eggs were collected within 6 hours post-fertilization (hpf). Dead embryos were identified, recorded, and removed prior to treatment. Subsequently, the culture medium was replaced with embryo medium containing the drug conditions. From 1 dpf to 5 dpf, zebrafish embryos were maintained in the compound-containing medium, which was refreshed daily to ensure consistent drug exposure. During this period, embryo/larval mortality and morphological abnormalities (as same as the **Health assessment**) were recorded at 24-hour intervals. The cumulative number of dead embryos and deformed larvae was used as the primary endpoint for toxicity evaluation.

Validation using Parkinsonism models

In the validation tests, zebrafish larvae were divided into three experimental groups including control, Parkinsonism models (MPTP/Rotenone/6-OHDA) and drug conditions, each one consisting of 10 animals in biological duplicates. Prior to all the animal experiments, we checked that at least 12 larvae could survive in each compound perfusion. To establish the Parkinsonism models, zebrafish larvae at 24 hours post-fertilization (hpf) were used. All treatments were performed in the dark at a constant temperature of 28°C.

MPTP-induced Parkinsonism model: MPTP was applied as the neurotoxin to induce dopaminergic neuron damage. MPTP was first dissolved in dimethyl sulfoxide (DMSO) to prepare the stock solution, and then further diluted in E3 medium to the final working concentration of 50 μM immediately before use. A vehicle control group treated with E3 medium containing an equal concentration of DMSO was

included to control for any potential effect of the solvent. The culture medium was changed daily throughout the entire modeling period.

Rotenone -induced Parkinsonism model: Rotenone was used as the neurotoxin to induce dopaminergic neuron damage. A stock solution of rotenone was prepared in dimethyl sulfoxide (DMSO) and further diluted in E3 medium to the final working concentration (10 μg/L) immediately before use. The vehicle control group received E3 medium with the corresponding concentration of DMSO. All treatments were performed in the dark, as rotenone is photosensitive. The medium was refreshed daily during the 96-hour exposure period to maintain a stable chemical environment.

6-OHDA-induced Parkinsonism model: 6-Hydroxydopamine (6-OHDA) was used as the neurotoxin to induce dopaminergic neuron damage. A fresh working solution of 6-OHDA was prepared immediately before use in E3 medium, protected from light at all times. Ascorbic acid was added to the working solution as an antioxidant to prevent the auto-oxidation of 6-OHDA. The final concentration of 6-OHDA was 250 μM, a concentration that ensures a high survival rate of the larvae while reliably inducing dopaminergic neuron damage and Parkinsonian-like motor deficits. A vehicle control group was treated with E3 medium containing an equal concentration of ascorbic acid alone to exclude any potential effects of the antioxidant. All incubation was performed under light-protected conditions, and the medium was changed daily during the exposure period to maintain a stable chemical environment, providing a reliable model for subsequent drug efficacy evaluation.

All the validation in the test group was performed using two drug treatment schemes, including co-treatment and post-treatment (Fig. 6a&7a). In the co-treatment scheme, candidate compounds and the corresponding neurotoxins (MPTP, rotenone, or 6-OHDA) were added together at 24 hpf and maintained until 5 dpf. In the post-treatment scheme, larvae were first exposed to the corresponding neurotoxin beginning at 24 hpf. After 48 hours of toxin exposure, candidate compounds were introduced at 72 hpf, while toxin exposure continued until 5 dpf. To be noted, all the Parkinsonism modeling procedures and prolonged drug exposures were performed in standard culture dishes. At 5 dpf, larvae were then transferred into the FD system through the droplet-generating chip and loaded into the trapping chips for behavioral assays and neural imaging: trapping chip I for behavioral recording (freely moving larvae in droplets), trapping chip II for dorsal confocal imaging of DC2/4 cells.

Locomotor activity analysis in the validation tests

The locomotor activity traces of the larvae in the droplets were recorded in real time over the experimental period. Larval locomotor trajectories were tracked frame by frame using the Animal Tracker plugin in ImageJ software, yielding sequential spatial coordinates (x_i, y_i) for each larva over the entire imaging session (i = 1, 2, ..., n, where n denoted the total number of video frames). All trajectory data were processed and analyzed with custom Python scripts. Three key behavioral parameters were calculated as follows:

(1) Total number of movements (N_{move}; Fig. 6f) was counted using a predefined displacement threshold d_{th} to define valid locomotor events:

$$N_{move} = \sum_{j=1}^{n-1} \begin{cases} 1, \sqrt{\left\|x_{j+1} - x_j\right\|^2 + \left(y_{j+1} - y_j\right)^2} > d_{th} \\ 0, otherwise \end{cases}$$

where d_{th} is the minimum displacement threshold for scoring a movement, and *n* is the total number of video frames.

(2) Total movement area (S_{total}, μm²; Fig. 6g) was determined as the area of the minimum bounding rectangle constructed from the extreme coordinates of the entire locomotor trajectory:

$$S_{total} = \left(x_{max} - x_{min}\right) \times \left(y_{max} - y_{min}\right)$$

where x_{max} and x_{min} were the maximum and minimum values of the x-coordinate, and y_{max} and y_{min} were the maximum and minimum values of the y-coordinate across the entire observation period.

(3) Distance moved per 30 seconds (D_{30S}, μm; Fig. 6h–k) was defined as the cumulative Euclidean distance traveled within each 30-second interval:

$$D_{30S} = \sum_{j=1}^{m} \sqrt{\left(x_{j+1} - x_j\right)^2 + \left(y_{j+1} - y_j\right)^2}$$

where *m* was the number of video frames in a 30-second window, and $\left(x_j, y_j\right)$ represented the spatial coordinates of the larva at frame *j*.

DA neuron counting

All imaging parameters, including objective magnification, laser intensity, gain, and offset, were held constant across all groups. Only cells with clearly defined, bright cell bodies and intact morphology were included in the analysis. The identification of the DC2/4 neurons was based on their anatomical positions, characteristic soma morphology, and relationships to surrounding anatomical landmarks. Specifically, DC2 neurons were identified as large, pear-shaped or oval GFP-positive somata located in the anterior region of central PT. DC4 neurons were identified as corresponding large GFP-positive somata in the posterior region of central PT, separated from DC2 by a narrow anatomical gap. The detailed anatomical locations were indicated in Fig. 7b. Other neighboring GFP-positive neuronal populations were excluded from quantification based on their distinct anatomical positions and morphological characteristics. These included DC1 cells near the ventral thalamus/PT boundary, DC3 cells associated with the paraventricular organ (PVO), and other hypothalamic GFP-positive populations.

Quantification was performed manually using serial confocal Z-stacks images (**Supplementary Figure S24**). Only GFP-positive cells with clearly delineated and independent somata located within the defined DC2 or DC4 anatomical boundaries were included. Isolated neuronal fibers, overlapping signals, and

ambiguous cellular structures were excluded. Serial optical sections were examined to avoid counting the same cell more than once across different imaging planes. Importantly, the quantification was performed under blinded conditions. An investigator who did not acquire the images assigned arbitrary codes to the confocal image stacks. A second investigator subsequently performed the manual counting without knowledge of the experimental groups. Treatment identities were unmasked only after all cell counts had been completed and recorded.

Statistical analysis

Statistical analyses were performed using SPSS Statistics 25 (IBM Corp., Armonk, NY). For the bar chart and curve graph, error bars indicated standard error of mean (s.e.m). For the box plots, the vertical centerline indicated the median, while the width of the box and error bar represented the interquartile range (IQR) and 1.5 times the IQR, respectively. One-way analysis of variance (ANOVA) was used to calculate differences between the two groups. Differences were considered statistically significant at $*p < 0.05$, $**p < 0.01$, $***p < 0.001$ and $****p < 0.0001$, “ns” indicated no significant difference by one-way analysis of variance (ANOVA). Unless otherwise specified, the data was shown as means ± s.e.m.

Data availability

The primary data that support the findings of this study are available from the corresponding author upon request.

Code availability

The custom codes and analysis scripts supporting this study were openly available in the GitHub repository (https://github.com/Jiaodashenshen/CNSDIP).

Declarations

Competing financial interests

The authors declare no conflict of interest.

Author Contributions

X.L. conceived and coordinated the project. Y.Z. and K.J. designed and fabricated the microfluidic system, performed the high-throughput drug screening and analyzed the data. X.D. and K.J. developed the computational tools and performed the informatic analysis. G.L. developed the automatic control system. K.Z., Z.Z. and T.C. contributed to validation parts. J.D., Z.Z., Y.Z. and B.X. contributed to data processing and helped with zebrafish maintainance. Y.Z., K.J., G.L., H.L. and X.L. wrote the manuscript.

Acknowledgment

We express our sincere gratitude to Prof. Jiulin Du (Institute of Neuroscience, Center for Excellence in Brain Science & Intelligence Technology, Chinese Academy of Sciences) and Prof. Bo Zhang (Key Laboratory of Cell Proliferation and Differentiation of the Ministry of Education, College of Life Sciences, Peking University) for kindly providing the transgenic line *Tg(elavl3:H2B-GCaMP6f)* (which was originally from the Ahrens Lab at Janelia Research Campus, Howard Hughes Medical Institute), and *ET(vmat2:GFP)*. We also thank Prof. Li Xiaoquan (School of Medicine, Sun Yat-sen Univeristy) for his inspiring discussion about this project. This work was supported by the National Natural Science Foundation of China (82372088, 82425104, 82203192), the National Natural Science Foundation of Guangdong Province (2025B1515020035), the Shanghai Municipal Education Commission (2024AI01014), the Shenzhen Science and Technology Program (202206193000001, 20220816161126002), the Postdoctoral Science Foundation of China (2021TQ0382, 2022M723669).

References

1. Pangalos MN, Schechter LE, Hurko O (2007) Drug development for CNS disorders: strategies for balancing risk and reducing attrition. Nat Rev Drug Discov 6:521–532
2. Wong ML, Licinio J (2004) From monoamines to genomic targets: a paradigm shift for drug discovery in depression. Nat Rev Drug Discov 3:136–151
3. Agid Y et al (2007) How can drug discovery for psychiatric disorders be improved? Nat Rev Drug Discov 6:189–201
4. Loscher W, Klitgaard H, Twyman RE, Schmidt D (2013) New avenues for anti-epileptic drug discovery and development. Nat Rev Drug Discov 12:757–776
5. Schapira AH et al (2006) Novel pharmacological targets for the treatment of Parkinson's disease. Nat Rev Drug Discov 5:845–854
6. Ghannad-Rezaie M, Eimon PM, Wu Y, Yanik MF (2019) Engineering brain activity patterns by neuromodulator polytherapy for treatment of disorders. Nat Commun 10:2620
7. Hyman SE (2012) Revolution stalled. Sci Transl Med 4:155cm111
8. Rennekamp AJ et al (2016) sigma1 receptor ligands control a switch between passive and active threat responses. Nat Chem Biol 12:552–558
9. Tang M et al (2022) Fish Capsules: A System for High-Throughput Screening of Combinatorial Drugs. Adv Sci (Weinh) 9:e2104449
10. Yu M et al (2024) Deep learning large-scale drug discovery and repurposing. Nat Comput Sci 4:600–614
11. Jayatunga MKP, Xie W, Ruder L, Schulze U, Meier C (2022) AI in small-molecule drug discovery: a coming wave? Nat Rev Drug Discov 21:175–176
12. Terwilliger TC et al (2024) AlphaFold predictions are valuable hypotheses and accelerate but do not replace experimental structure determination. Nat Methods 21:110–116

13. Diaz-Holguin A et al (2024) AlphaFold accelerated discovery of psychotropic agonists targeting the trace amine-associated receptor 1. Sci Adv 10:eadn1524
14. Eduati F et al (2018) A microfluidics platform for combinatorial drug screening on cancer biopsies. Nat Commun 9:2434
15. Mathur L et al (2022) Combi-seq for multiplexed transcriptome-based profiling of drug combinations using deterministic barcoding in single-cell droplets. Nat Commun 13:4450
16. Lin X et al (2015) High-throughput mapping of brain-wide activity in awake and drug-responsive vertebrates. Lab Chip 15:680–689
17. Lin X et al (2018) High-throughput brain activity mapping and machine learning as a foundation for systems neuropharmacology. Nat Commun 9:5142
18. Hassani S, Esmaeili A (2024) The neuroprotective effects of Ferulic acid in toxin-induced models of Parkinson's disease: a review. Ageing Res Rev 97:102299
19. Sathiya S et al (2013) Telmisartan attenuates MPTP induced dopaminergic degeneration and motor dysfunction through regulation of α-synuclein and neurotrophic factors (BDNF and GDNF) expression in C57BL/6J mice. Neuropharmacology 73:98–110
20. Meng F et al (2017) Neuroprotective effect of matrine on MPTP-induced Parkinson's disease and on Nrf2 expression. Oncol Lett 13:296–300
21. Zhao J et al (2025) Palmatine Ameliorates Motor Deficits and Dopaminergic Neuron Loss by Regulating NLRP3 Inflammasome through Mitophagy in Parkinson's Disease Model Mice. Mol Neurobiol 62:2250–2263
22. Doyle JM, Croll RP (2022) A critical review of zebrafish models of Parkinson’s disease. Front Pharmacol 13:835827
23. Maegawa H, Niwa H (2021) Generation of mitochondrial toxin rodent models of Parkinson’s disease using 6-OHDA, MPTP, and rotenone. Experimental models of Parkinson’s disease, pp 95–110
24. Lam CS, Korzh V, Strahle U (2005) Zebrafish embryos are susceptible to the dopaminergic neurotoxin MPTP. Eur J Neurosci 21:1758–1762
25. Sallinen V et al (2009) MPTP and MPP+ target specific aminergic cell populations in larval zebrafish. J Neurochem 108:719–731
26. Feng CW, Wen ZH, Huang SY et al (2014) Effects of 6-hydroxydopamine exposure on motor activity and biochemical expression in zebrafish (Danio rerio) larvae. Zebrafish 11(3):227–239
27. Ranasinghe T, Seo Y, Park HC et al (2024) Rotenone exposure causes features of Parkinsons disease pathology linked with muscle atrophy in developing zebrafish embryo. J Hazard Mater 480:136215
28. Bai AD, McKenna S, Wise H et al (2022) Association of linezolid with risk of serotonin syndrome in patients receiving antidepressants. JAMA Netw Open 5(12):e2247426
29. Lawrence KR, Adra M, Gillman PK (2006) Serotonin toxicity associated with the use of linezolid: a review of postmarketing data. Clin Infect Dis 42(11):1578–1583

30. McDaniel WW (2013) Antidepressant activity of linezolid. J Neuropsychiatry Clin Neurosci 25:E59–E59
31. Schneider F, Gessner A, El-Najjar N (2022) Efficacy of vancomycin and meropenem in central nervous system infections in children and adults: current update. Antibiotics 11:173
32. Jamroz-Wiśniewska A, Bełtowski J, Wójcicka G, Bartosik-Psujek H, Rejdak K (2020) Cladribine treatment improved homocysteine metabolism and increased total serum antioxidant activity in secondary progressive multiple sclerosis patients. *Oxid Med Cell Longev* 1654754 (2020)
33. Michel PP, Hirsch EC, Hunot S (2016) Understanding Dopaminergic Cell Death Pathways in Parkinson Disease. Neuron 90:675–691
34. Li X et al (2022) Anti-Parkinson's disease activity of sanghuangprous vaninii extracts in the MPTP-induced zebrafish model. ACS Chem Neurosci 13:330–339
35. Wen L, Wei W, Gu W et al (2008) Visualization of monoaminergic neurons and neurotoxicity of MPTP in live transgenic zebrafish. Dev Biol 314(1):84–92
36. Ilin VA, Bai Q, Watson AM, Volgushev M et al (2021) Mechanism of Pacemaker Activity in Zebrafish DC2/4 Dopaminergic Neurons. J Neurosci 41(18):4141–4157
37. Du Y, Guo Q, Shan M et al (2016) Spatial and Temporal Distribution of Dopaminergic Neurons during Development in Zebrafish. Front Neuroanat 10:115
38. Kalia LV, Lang AE (2015) Parkinson's disease. lancet 386(9996):896–912
39. Ahrens MB, Orger MB, Robson DN, Li JM, Keller PJ (2013) Whole-brain functional imaging at cellular resolution using light-sheet microscopy. Nat Methods 10:413–420
40. Pardo-Martin C et al (2010) High-throughput in vivo vertebrate screening. Nat Methods 7:634–636
41. Camp JG, Lukonin I (2022) Single-cell, single-organoid phenotypic landscapes. Nat Methods 19:280–281
42. Frey O, Misun PM, Fluri DA, Hengstler JG, Hierlemann A (2014) Reconfigurable microfluidic hanging drop network for multi-tissue interaction and analysis. Nat Commun 5:4250
43. Saint-Sardos A et al (2020) High-Throughput Measurements of Intra-Cellular and Secreted Cytokine from Single Spheroids Using Anchored Microfluidic Droplets. Small 16:e2002303
44. Benz M et al (2020) A combined high-throughput and high-content platform for unified on-chip synthesis, characterization and biological screening. Nat Commun 11:5391
45. Benz M, Molla MR, Boser A, Rosenfeld A, Levkin PA (2019) Marrying chemistry with biology by combining on-chip solution-based combinatorial synthesis and cellular screening. Nat Commun 10:2879
46. Utharala R, Grab A, Vafaizadeh V et al (2022) A microfluidic Braille valve platform for on-demand production, combinatorial screening and sorting of chemically distinct droplets. Nat Protoc 17:2920–2965
47. McKinley ET et al (2005) Neuroprotection of MPTP-induced toxicity in zebrafish dopaminergic neurons. Mol Brain Res 141:128–137

48. Song SW et al (2019) One-Step Generation of a Drug-Releasing Hydrogel Microarray-On-A-Chip for Large-Scale Sequential Drug Combination Screening. Adv Sci (Weinh) 6:1801380
49. Pardo-Martin C et al (2013) High-throughput hyperdimensional vertebrate phenotyping. Nat Commun 4:1467
50. Xiao J, Glasgow E, Agarwal S (2020) Zebrafish Xenografts for Drug Discovery and Personalized Medicine. Trends Cancer 6:569–579
51. Aubry G, Milisavljevic M, Lu H (2022) Automated and Dynamic Control of Chemical Content in Droplets for Scalable Screens of Small Animals. Small 18:e2200319
52. Lucchetta EM, Lee JH, Fu LA, Patel NH, Ismagilov RF (2005) Dynamics of Drosophila embryonic patterning network perturbed in space and time using microfluidics. Nature 434:1134–1138
53. Dunn TW, Mu Y, Narayan S et al (2016) Brain-wide mapping of neural activity controlling zebrafish exploratory locomotion. Elife 5:e12741
54. Kawashima T, Zwart MF, Yang CT et al (2016) The serotonergic system tracks the outcomes of actions to mediate short-term motor learning. Cell 167(4), 933–946. e20
55. Feng W, Ueda E, Levkin PA (2018) Droplet Microarrays: From Surface Patterning to High-Throughput Applications. Adv Mater 30:e1706111
56. Bruni G et al (2016) Zebrafish behavioral profiling identifies multitarget antipsychotic-like compounds. Nat Chem Biol 12:559–566

Figures

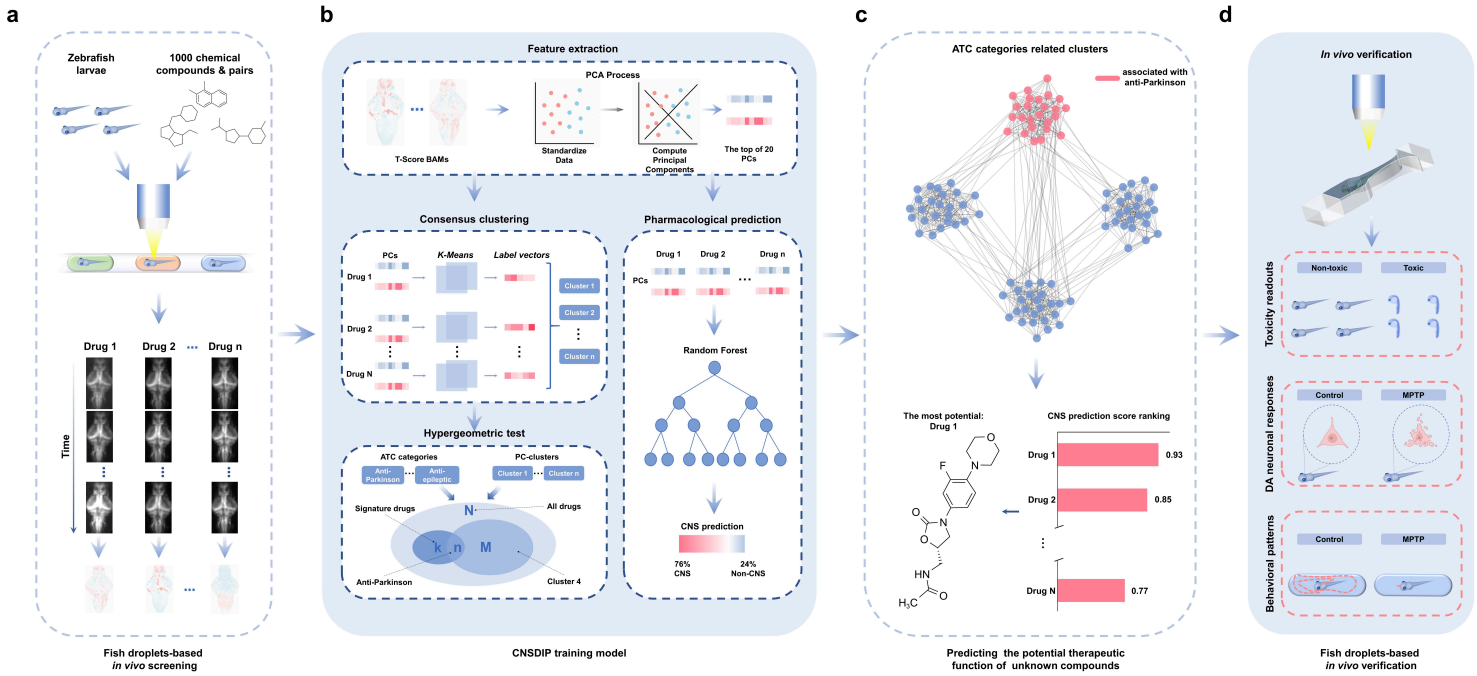

Figure 1

Framework of *in vivo* profiling for large-scale drug discovery and repurposing. (a-d) The framework comprised four components: acquisition of whole-brain activity data from zebrafish larvae exposed to drug conditions using a droplet microfluidics-based automatic system **(a)**; machine-learning-based CNSDIP training model involved extracting features from image sequences using T-score tests and principle component analysis, functional identification and ranking based on consensus clustering, hypergeometric tests and Random Forest prediction **(b)**; CNSDIP identified and ranked drug conditions with high anti-Parkinson therapeutic potential **(c)**; and *in vivo* functional validation of the drug candidates using the FD system, including evaluations of toxicity readouts, DA neuronal patterns, and behavioral patterns **(d)**.

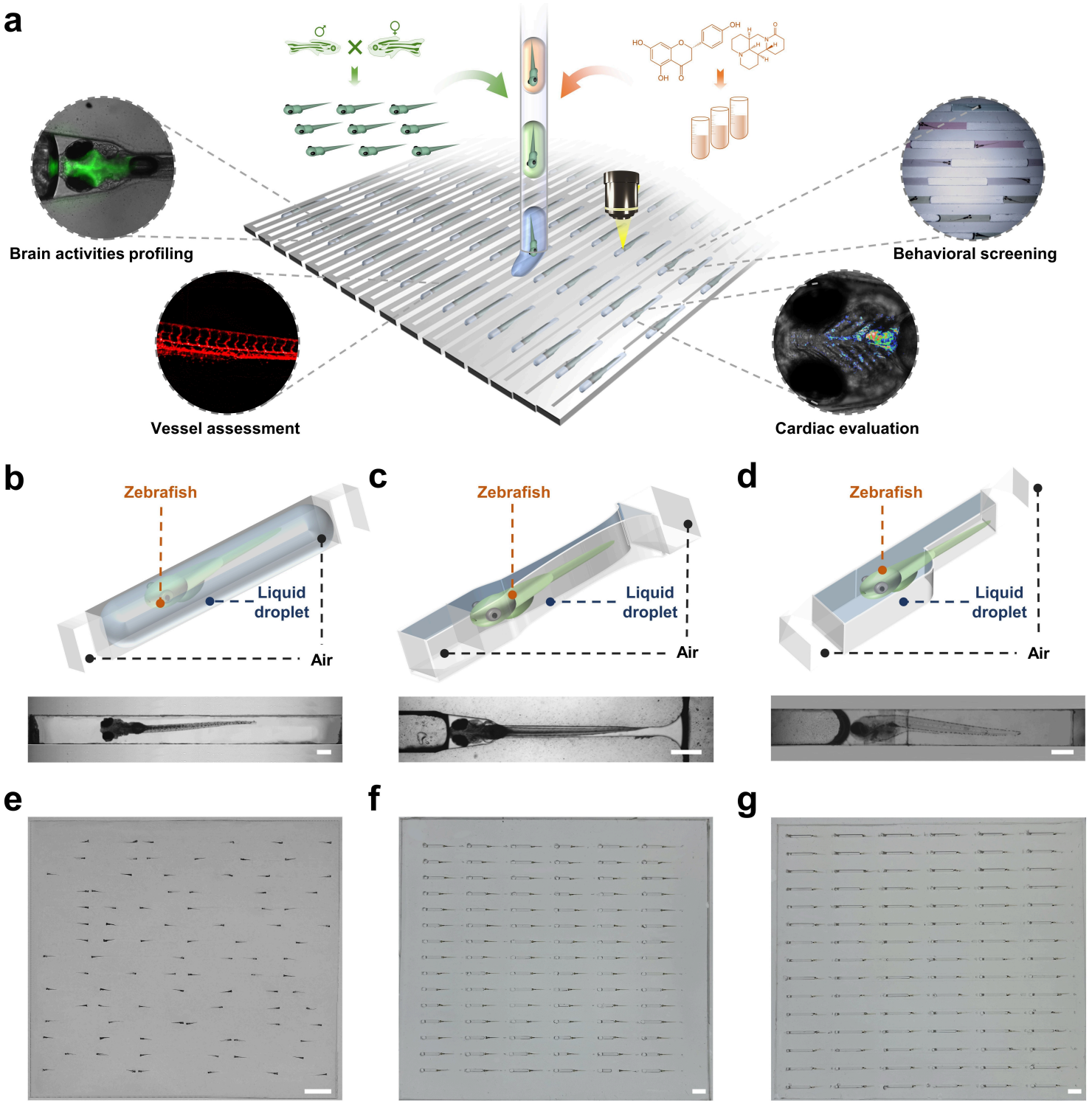

Figure 2

High-throughput and high-content *in vivo* screens enabled by the Fish-in-Droplets (FD) System. (a) The FD system enabled large-scale capsuling of single zebrafish larvae in droplets for further on-chip brain-wide activities profiling, cardiac evaluation, blood assessment, and behavioral screening. **(b-d)** Microscopic images and schematic diagrams showing a droplet containing an immobilized larva in the trapping chip I **(b)**, II **(c)**, III **(d)**. Scale bar, 500 μm. **(e-f)** Images showing the trapping chip I **(e)**, II **(f)**, III **(g)**. Scale bar, 2 mm.

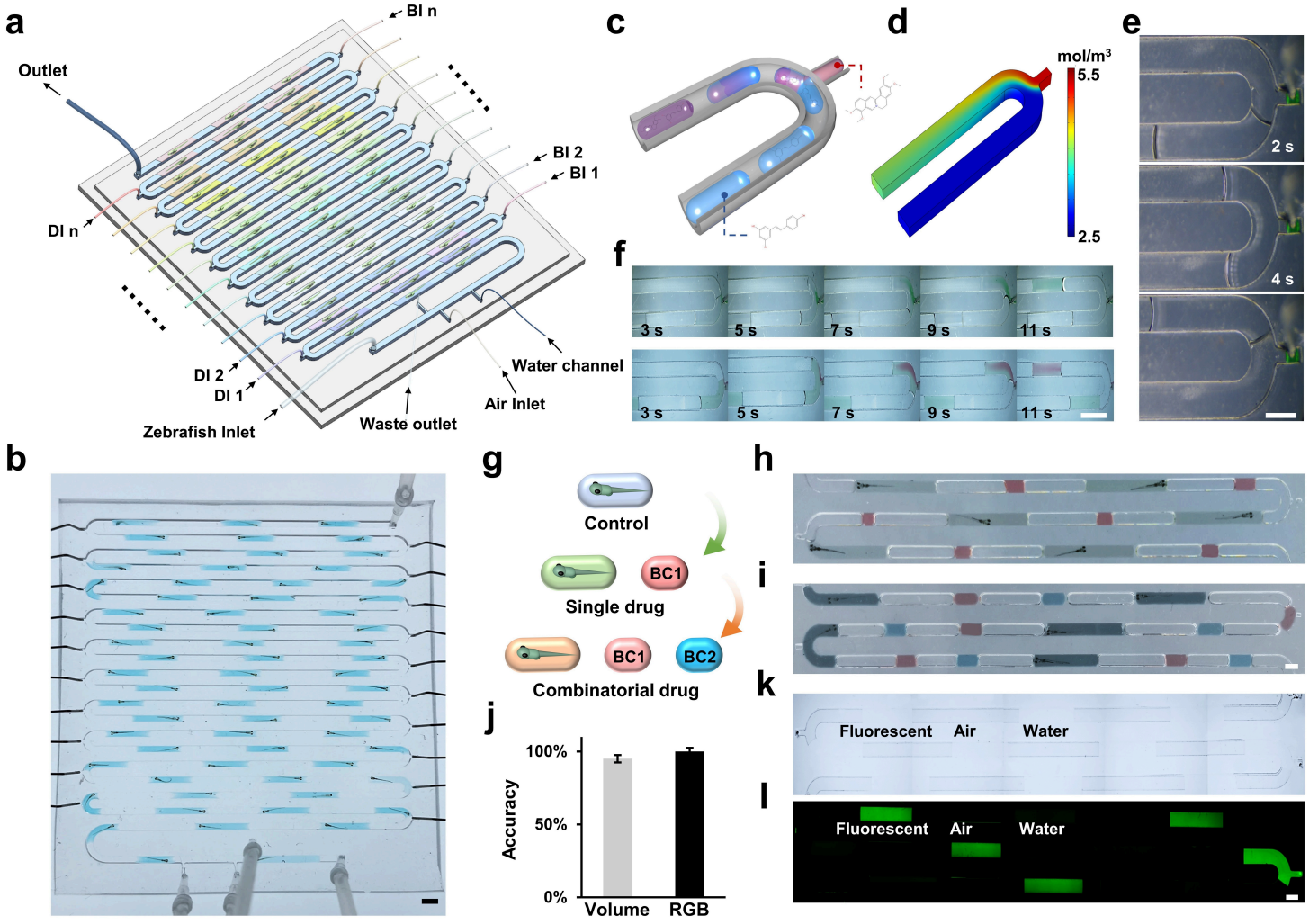

Figure 3

Large-scale generation of zebrafish droplets. (a-b) Schematic diagram **(a)** and photograph **(b)** of the setup of the droplet-generating chip. Scale bar, 3 mm. **(c)** Schematic representation of chemical compound addition process in the droplet-generation microfluidic chip. The red and blue dyes indicate different chemical compounds respectively. (**d**) Simulation results showing the drugs squeezing. **(e)** Representative microscopic images of a thin layer of air at each injection nozzle. Scale bar, 1 mm. **(f)** Representative image sequences of compounds addition. The upper process images indicated the injection of a single compound (green dye) in a microdroplet. The sequence below represents the injection of compound combinations (green and red dyes). Scale bar, 2 mm. **(g)** Schematic showing the barcoding strategy. Single compounds and combinations are automatically generated with each specific barcodes (BCs). **(h-i)** Images showing an addition of single compound with red BC **(h)** and an addition of compound combinations with BCs in the FD system **(i)**. Scale bar, 1.5 mm. **(j)** Bar chart of the accuracy assessment of drug information decoding based on RGB values and volume of the BCs. **(k-l)** Bright field images and fluorescence images showing no cross-contamination of drugs between droplets were observed in the droplet-generating chip. Scale bar,1 mm.

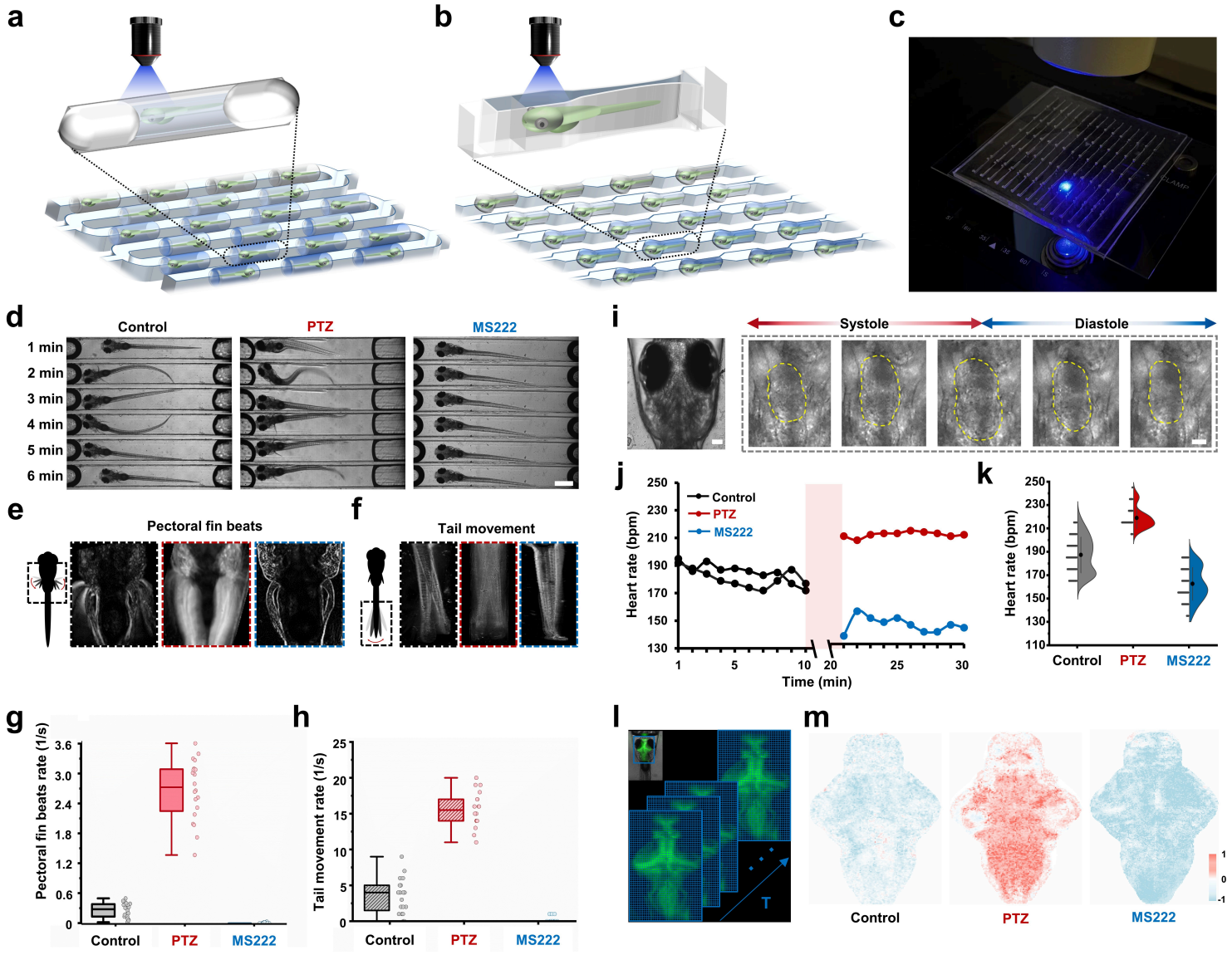

Figure 4

Multiplexed *in vivo* profiling of compounds using the FD system.(**a**) Schematic showing the set-up for behavioral monitoring the animals in the droplet-generation chip. (**b-c**) Schematic (**b**) and image (**c**) showing the set-up for specific-organ imaging of the larvae in the trapping chip. (**d**) Representative image sequences showing the behavioral responses of the larvae induced by E3 water (control group), PTZ and MS222. Scale bar, 1 mm. (**e-h**) Representative stacked images (**e-f**) and quantitative analysis (**g-h**) showing the behavioral changes of the larvae with different treatments (black, red and blue dashed squares indicated the control, PTZ and MS222 groups respectively). (**i**) Representative image sequences showing the volume change of the heart during a contraction-relaxation cycle in wild-type zebrafish in a droplet in the trapping chip. Scale bar, 100 μm. (**j**) Representative heart rate fluctuation with different compound treatments. (**k**) Violin plots illustrating the heartrate changes of the larvae under compound treatments. (**l**) Illustration of the brain activity mapping using the trapping chip coupling with *Tg(elavl3: H2B-GCaMP6f)* transgenic zebrafish larvae. (**m**) The T-score brain activity maps showing the neural modulation effects of different compounds.

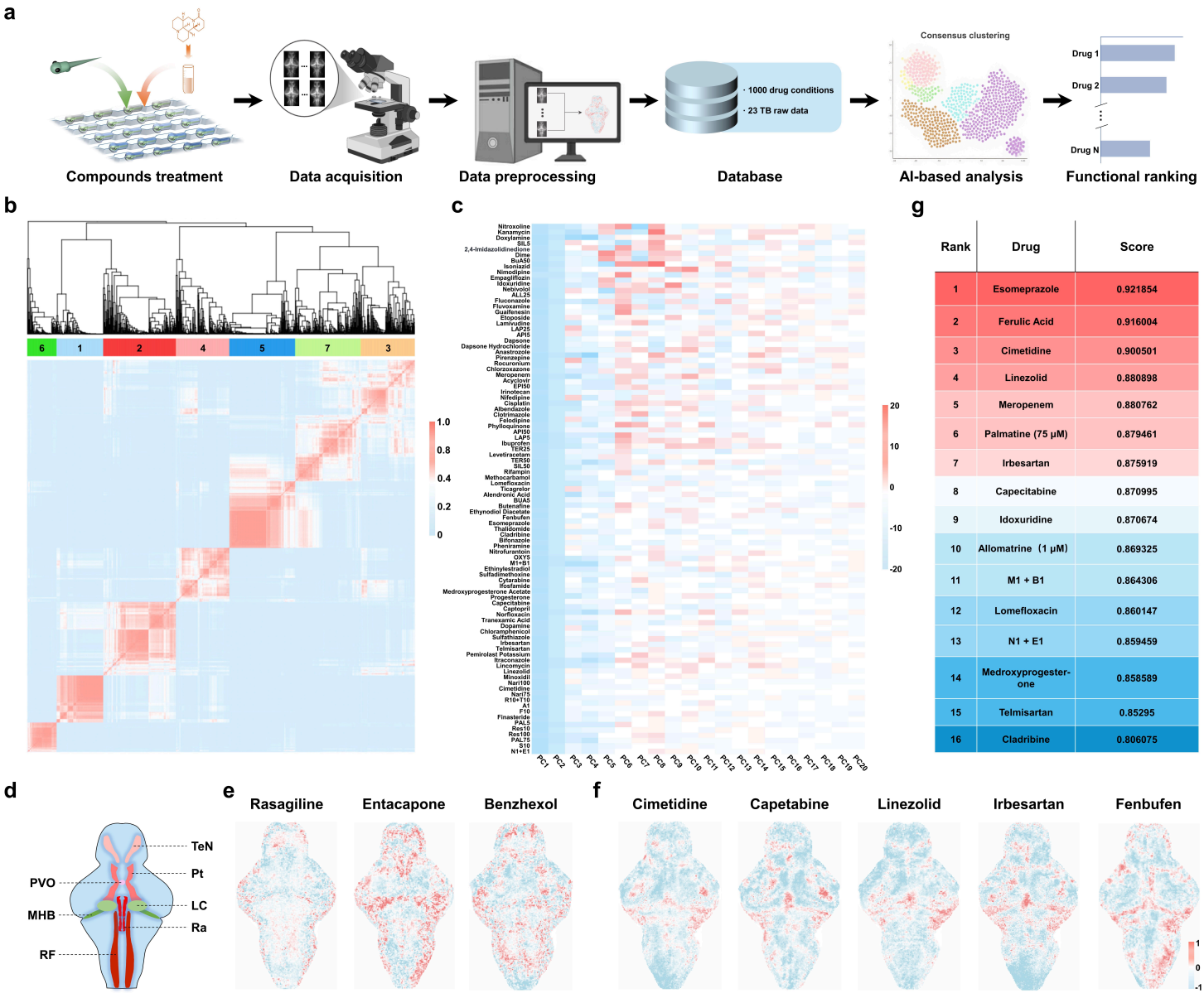

Rank	Drug	Score
1	Esomeprazole	0.921854
2	Ferulic Acid	0.916004
3	Cimetidine	0.900501
4	Linezolid	0.880898
5	Meropenem	0.880762
6	Palmatine (75 μM)	0.879461
7	Irbesartan	0.875919
8	Capecitabine	0.870995
9	Idoxuridine	0.870674
10	Allomatrine（1 μM）	0.869325
11	M1 + B1	0.864306
12	Lomefloxacin	0.860147
13	N1 + E1	0.859459
14	Medroxyprogester-one	0.858589
15	Telmisartan	0.85295
16	Cladribine	0.806075

Figure 5

Functional prediction of drug conditions using CNSDIP. (a) Schematic representation of dataset acquisition from 1,000 drug conditions using the FD system. **(b)** Consensus clustering identified 7 phenotypic T-score brain activity map (T-score BAM) clusters. The heat map was the consensus matrix illustrating the frequency of the scenario that two compounds in a pair were clustered together. The color of the heat map was proportional to the frequency scores of the consensus matrix, ranging from 0 to 1. **(c)** The 20-dimensional pheno-prints (featured by the top 20 principal components) for all the tested drug conditions in the cluster 4. **(d)** Schematics showing the representative brain regions related to the dopaminergic system in zebrafish larvae. **(e-f)** T-score BAMs of representative in-cluster anti-Parkinson's drugs **(e)** and the predicted in-cluster drug conditions **(f)**. **(g)** Probability ranking generated based on the CNSDIP model.

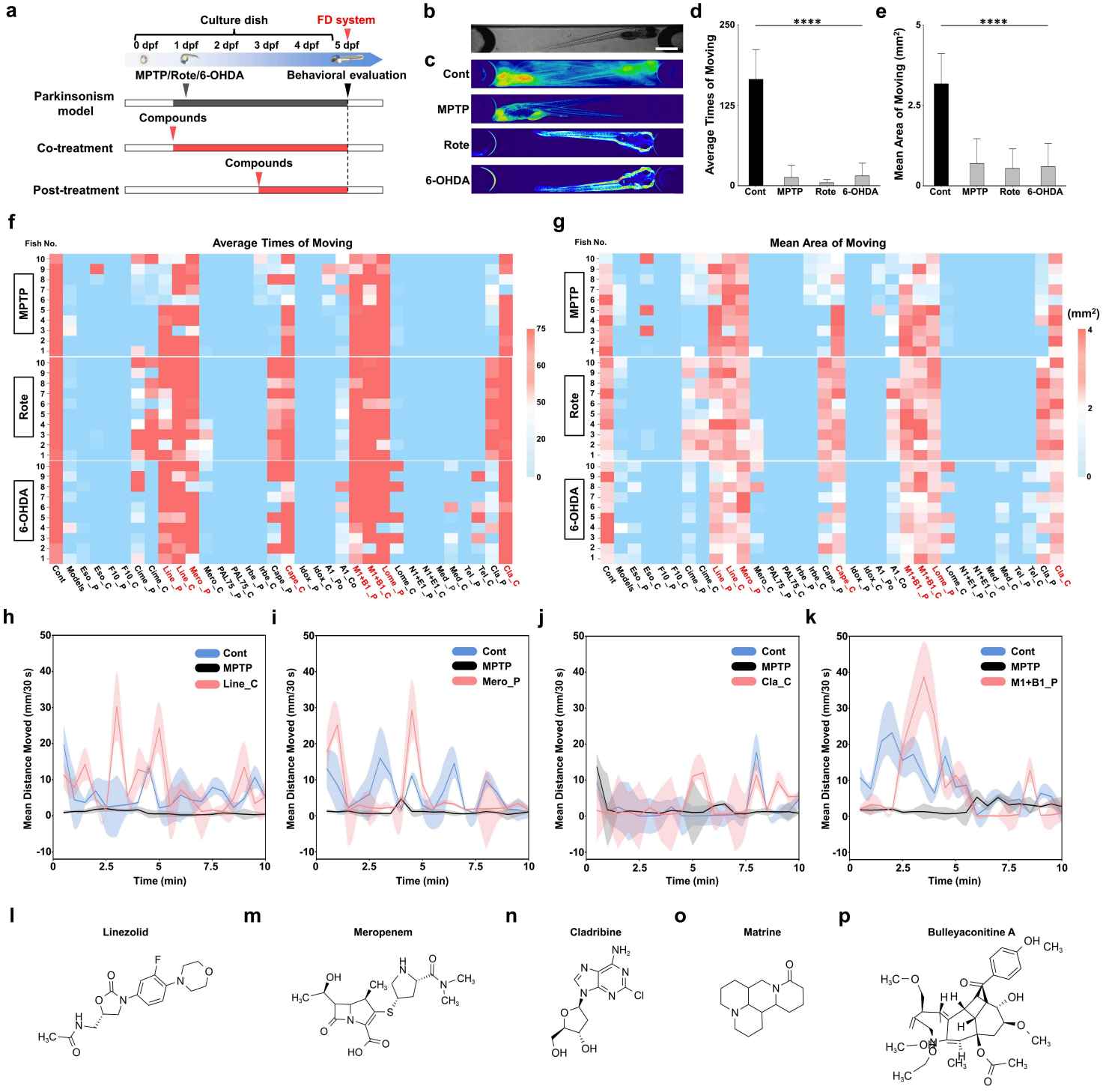

Figure 6

Behavioral validation of the candidates using the FD system. (**a**) Two treatment schemes, including co-treatment and post-treatment, were employed. All modeling procedures and drug exposures were performed in standard culture dishes. At 5 dpf, larvae were then transferred into the FD system for behavioral evaluation. (**b-c**) The representative image (**b**) of a Parkinsonian larva and heatmaps (**c**) of time spent of the animals in the droplets in the trapping chip I during within 10 minutes. Scale bar, 1 mm (**d-e**). Mean spontaneous moving times (**d**) and area of movement (**e**) of the animals recorded in the

control group and Parkinsonism model groups. ****p< 0.0001, by one-way analysis of variance (ANOVA), n = 10. (**f-g**) Heatmaps of statistical analysis of locomotion behaviors of Parkinsonian larvae in response to the identified top-ranked candidates in cluster 4 in post-treatment and co-treatment tests. (**h-k**) Representative traces of the induced locomotion behaviors of animals by exposure to linezolid (**h**), meropenem (**i**), cladribine (**j**), matrine paired with bulleyaconitine A (**k**). **(l-p)** Chemical structures of linezolid (**l**), meropenem (**m**), cladribine (**n**), matrine (**o**) and bulleyaconitine A (**p**).

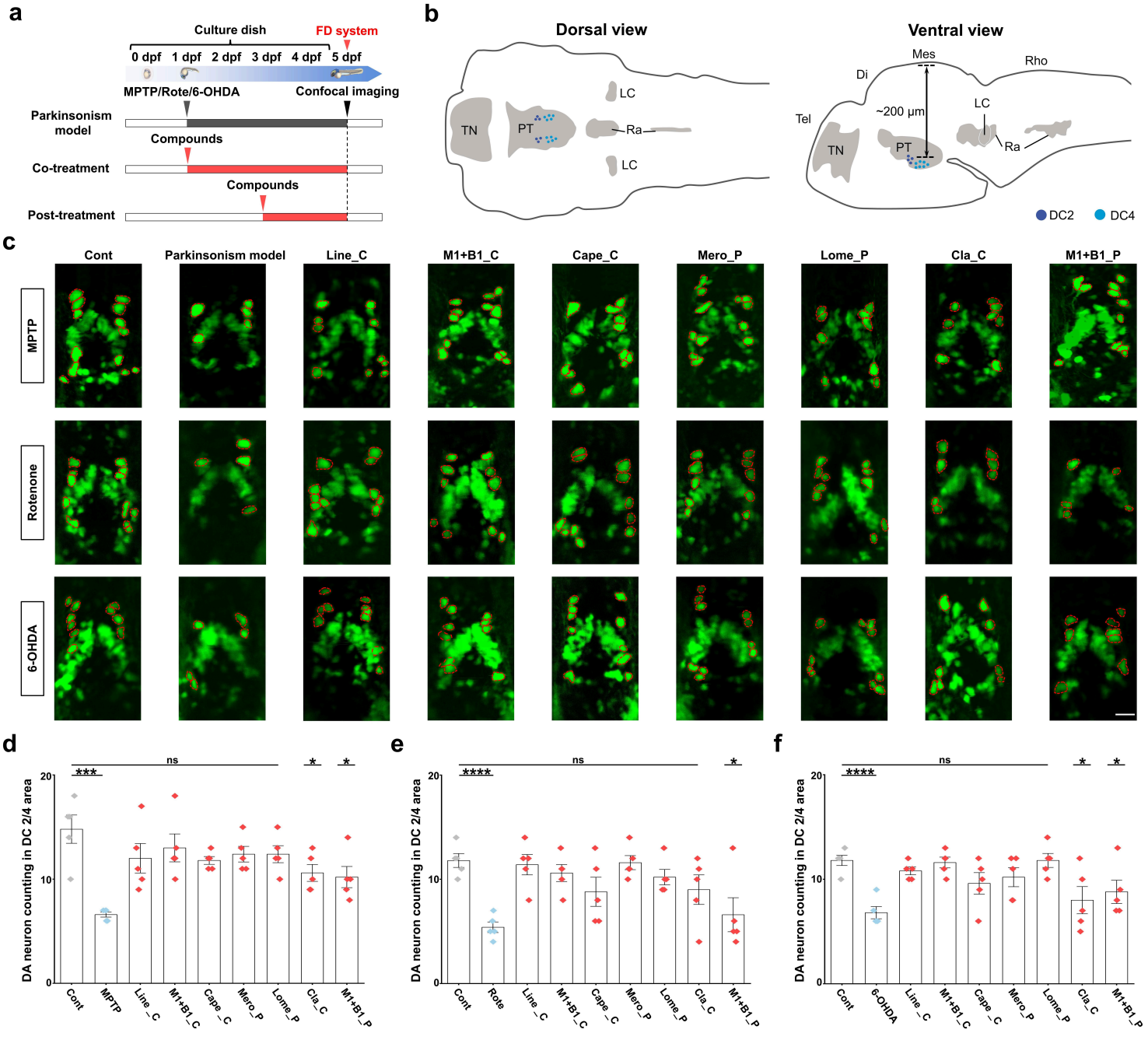

Figure 7

Evaluation of dopaminergic (DA) neuron integrity in *ET*(*vmat2:GFP*) zebrafish. (**a**) Two treatment schemes, including co-treatment and post-treatment, were employed. All modeling procedures and drug exposures were performed in standard culture dishes. At 5 dpf, larvae were then transferred into the FD

system for confocal imaging. **(b)** Schematic illustration showing the anatomical locations of DC2/4 in the brain of a 5-dpf zebrafish from dorsal and ventral views. (**c**) Representative confocal images of DC2/4 neurons (outlined by red dashed circles) in the posterior tuberculum (PT) regions in *ET(vmat2:GFP)* zebrafish larvae following drug treatments on three different Parkinsonism models (MPTP, Rotenone and 6-OHDA-induced). Scale bar, 25 μm. (**d-f**) Quantification of GFP-labeled DC2/4 neuron numbers after drug treatments in the MPTP-induced (**d**), Rotenone-induced (**e**) and 6-OHDA-induced (**f**) Parkinsonism models. Error bars indicated standard error of the mean (s.e.m.). *p< 0.05, **p < 0.01, ***p < 0.001, ****p < 0.0001, “ns” indicated no significance, by one-way analysis of variance (ANOVA), n = 5.

Supplementary Files

This is a list of supplementary files associated with this preprint. Click to download.

- SupplementaryMovie2.mp4
- SupplementaryMovie3.mp4
- SupplementaryMaterials20261118.docx
- SupplementaryMovie5.mp4
- SupplementaryMovie1.mp4
- SupplementaryMovie4.mp4